Diamond platforms for nanoscale photonics and metrology

Diamond platforms for nanoscale photonics and metrology

a dissertation presented
by
Brendan John Shields
to
The Department of Physics

in partial fulfillment of the requirements
for the degree of
Doctor of Philosophy
in the subject of
Physics

Harvard University
Cambridge, Massachusetts
April 2014

Thesis advisor: Professor Mikhail D. Lukin Brendan John Shields

Diamond platforms for nanoscale photonics and metrology

Abstract

Observing and controlling solid state quantum systems is an area of intense research in quantum science today. Such systems offer the natural advantage of being bound into a solid device, eliminating the need for laser cooling and trapping of atoms in free space. These solid state "atoms" can interface directly with photonic channels designed to efficiently couple into larger networks of interacting quantum systems. With all of the tools of semiconductor fabrication technology available, the idea of scalable, chip-based quantum networks is a tantalizing prospect.

This thesis explores the basic interaction between a solid state emitter and its photonic environment. The environment can be designed to concentrate and trap light for coherent light-matter interactions that fundamentally alter the emitter's behavior, or it can be designed to efficiently channel light into an observing device. Both aspects are investigated here. Working with single nitrogen-vacancy (NV) color centers in diamond, we engineer their surroundings to incorporate them into photonic crystal cavities and nanophotonic wavguide devices. NV-cavity coupling is demonstrated for hybrid systems, where the cavity is fabricated from gallium phosphide, and for monolithic devices fabricated entirely from diamond. Enhancement of the NV zero phonon line emission by a factor of 7 is shown. Additionally, NV centers are incorporated into diamond nanobeams for enhanced photon collection efficiency, enabling improvements

in nanoscale metrology. Precise control of the NV charge state and efficient conversion of the NV spin state to a charge state is demonstrated, further enhancing the NV's capabilities as a nanoscale sensor.

Contents

Listing of figures

Citations to previously published work

Some parts of this thesis have appeared previously in published articles.

Chapter 2 and Appendix A appeared previously in:

> "Deterministic Coupling of a Single Nitrogen Vacancy Center to a Photonic Crystal Cavity", Dirk Englund*, Brendan Shields*, Kelley Rivoire, Fariba Hatami , Jelena Vučković, Hongkun Park, and Mikhail D. Lukin, *Nano Letters* **2010** *10* (10), 3922-3926.

Chapter 3 appeared previously in:

> "Coupling of NV Centers to Photonic Crystal Nanobeams in Diamond", B. J. M. Hausmann*, B. J. Shields*, Q. Quan, Y. Chu, N. P. de Leon, R. Evans, M. J. Burek, A. S. Zibrov, M. Markham, D. J. Twitchen, H. Park, M. D. Lukin, and M. Lončar, *Nano Letters* **2013** *13* (12), 5791-5796.

*These authors contributed equally

To my parents.

Acknowledgments

In my time at Harvard I have been fortunate to have the opportunity to learn from many talented people. First and foremost I would like to thank my advisor, Misha, for his support and encouragement, and for giving me a kick in the rear at a few key junctures. Probably the most important thing I have learned in graduate school is to think critically about everything I do, and about why I am doing it. Misha creates that mentality in his group, and it is a special place to work as a result.

I would also like to thank my committee members, Hongkun Park, Ron Walsworth, and John Doyle, for their honest feedback and advice. To Hongkun, in particular, I owe a debt of gratitude for the impetus to start the new project on spin readout. John was a helpful outside voice on my committee for many years, and Ron's interest in and encouragement for my project have been much appreciated along the way.

Early on I had the opportunity to spend a summer working in the lab of Nancy Kleckner, who humored my interest in biology. I very much enjoyed my time spent in the bacteria lab, and I am very grateful for the patience and enthusiasm with which Nancy, Suckjun Joon, Aude Bourniquel, Romain Koszul, and especially Kate Mirkin, greeted my tenure in the lab.

Of course, as an experimentalist, I benefitted enormously from the many brilliant individuals with whom I shared my time in the Lukin lab: Alexey Akimov, Misho Ba-

jcsy, Erik Bauch, Steve Bennett, Ania Bleszynski Jayich, Jonatan Brask, Paola Cappellaro, Darrick Chang, Lily Childress, Nick Chisholm, Soonwon Choi, Yiwen Chu, Gurudev Dutt, Kristiaan De Greve, Nathalie de Leon, Dirk Englund, Ruffin Evans, Ofer Firstenberg, Mike Goldman, Garry Goldstein, Alexey Gorshkov, Mike Gullans, Mohammad Hafezi, Phil Hemmer, Jonathan Hodges, Sahand Hormoz, Liang Jiang, Eric Kessler, Shimon Kolkowitz, Peter Komar, Frank Koppens, Alex Kubanek, Georg Kucsko, Cristian Latta, Chris Laumann, Albert Lee, Lee Liu, Igor Lovchinsky, Peter Maurer, Jero Maze, Johannes Otterbach, Adi Pick, Peter Rabl, Alp Sipahigil, Arthur Safira, Alex Sushkov, Jeff Thompson, Tobias Tieke, Emre Togan, Alexey Trifonov, Quirin Unterreithmeier, Norman Yao, Tamara Zibrova, Sasha Zibrov, and Sasha Zibrov.

In the beginning, there was a man, and his name was Alexey Akimov. Or at least, that was how Misha introduced him to me. Alexey taught me everything I needed to know about confocal microscopy, second-order autocorrelation measurements, and even a few key Russian phrases. I especially admire his tireless work ethic, and I hope that in some small way I emulate his experimental fortitude.

Alexey and I worked on coupling NV centers to silver nanowires, along with Frank Koppens, Parag Deotare, and Chun Yu. Frank gave me plenty of practice with aligning optics, and Parag and Chun provided a lot of ideas and support on device assembly. At various times we were joined by Lily Childress, Jonathan Hodges, and Jero Maze, from whom I learned a lot of NV physics as well as bits and pieces of diamond lore. Everyone worked with a cheerful smile and a carefree laugh, and I have fond memories of our time together.

Eventually Dirk Englund convinced me that coupling NV centers to photonic crystals was going to be the next big thing, and we started working on that together.

Dirk taught me that sometimes it is best to pursue ten different solutions to a problem and run with whichever one turns out to work. I have never worked with someone so full of energy and ideas as he is, and his encouragement over the years continues to be much appreciated.

Sooner or later it became clear that we needed to move on from gallium phosphide cavities to an all-diamond approach, and this turned into a vibrant collaborative effort, consisting of Nathalie de Leon, Birgit Hausmann, Michael Burek, Yiwen Chu, and Ruffin Evans, along with additional guidance from Marko. Nathalie's organization kept the project on track, especially in those moments when it seems like nothing works. Birgit and Michael can do things in the clean room that I never would have believed possible, and their tireless and consistent work produced truly amazing diamond structures. Yiwen taught me everything I know about low temperature NV experiments, and a good deal of what I know about microwave spin manipulation, besides being a constant friend in the lab. Ruffin has been an eager student with steadfast patience and relentless inquisitiveness; his is a calm and measured presence at all times. Later on Kristiaan De Greve joined the project, and his experimental wisdom and attention to detail have been highly instructive.

Over the past year and a half, I embarked on a totally different experimental direction, delving into the spin and charge dynamics of the NV center, which behooved me to learn about NV spin manipulation. Fortunately, there is no better place for this than the Lukin group, and I had many instructive conversations with Shimon Kolkowitz, Peter Maurer, Georg Kucsko, Yiwen, Alp Sipahigil, Mike Goldman, Alex Kubanek, Igor Lovchinski, Nick Chisholm, Alex Sushkov, and Alexey Trifonov (and quite possibly a few others), over the course of which I came to understand the intimate details of spin readout noise. Nathalie contributed ideas and support on the

device geometry for high collection efficiency. Nobody contributed more to the effort to understand and to model the underlying processes than my friend and collaborator, Quirin Unterreithmeier. He worked out many of the details for modeling the photon statistics, and was invaluable in fitting and analyzing the results of the experiment. At the outset of my investigation of the NV charge state he urged me, first gently and then more insistently, to implement his LabScript Pro control software that greatly simplified the measurements. Besides his many practical contributions, Quirin's zeal and curiosity for all things scientific and otherwise, and especially his unabashed delight with certain curiosities of the English language, remain dear to my heart.

It is always a great help to run things by someone not directly involved with a project, and several individuals were frequent resources for such experimental advice. Jeff Thompson and Emre Togan, had often already solved whatever problem I was then dealing with. Sasha Zibrov, especially, was invaluable for his optics experience and contributed many custom parts to the experiment. If you ask nicely and have a good idea, he might just have an AOM for it. Tobias Tieke has been an enthusiastic friend, always with a fresh take on things and a wonderful clarity of thought, usually with a clever idea, and often over a beer. His faithful defense of the Dutch tractor pulling scene is laudable.

I've been very fortunate to be supported by the wonderful staff of the physics department, especially Joan Hamilton, Adam Ackerman, Silke Exner-Su, Jean O'Connor, Vickie Greene, Carol Davis, Sheila Ferguson, and Lisa Cacciabaudo.

Of course I learned as much outside of the lab as in it, and for that I have many friends to thank. In the office, my main chuvak Norm has been an ever present friend who seems always to understand what I am thinking and, more importantly, what I should be doing about it. His bank shot has been steadily improving, too. Just as

near and dear to my heart is my very talented pianist, Yiwen, who holds a special place in all my fondest memories of grad school. Our chamber group was sometimes joined by Adi Pick on the cello. Elsewhere in the department, Mike Kagan, Josh Dorr, Daniyar Nurgaliev, Tess Williams, Yat Shan Au, Yejin Huh, Vasily Dzyabura, Peter Blair, Deriba Olana, Kate Jensen, Jason Dowd, Tracy Slatyer, Max Metlitski, Vivek Venkatachalam, Phil Richerme, Christian Freudiger, and Garry Goldstein have all been good friends since orientation. Many friends from the outside world have touched my life throughout these years, especially Dasha Babushok and Clem McGrath, Halleh Balch, Giacomo Barbone, Katia Bertoldi and Giovanni Berlanda, Larry and Sara Mae Berman, Barb Bryant and Dave Yee, Michael Commons, Ali Crocker, Neil Dobbs, Stephen Granger-Bevan, Lori and Presto Huberman, Alex Jospe and Ed Despard, Minda Lekaveckas, Ian Smith, Ross Smith and Sam Saeger, Lisa Snyder, Dean Sturtevant, Ed Su, and Pia and Mark Webb. And last but not least, my family, Ian, Pat, Catherine and Michael, who have been there all along.

Many thanks to all of you.

Chapter 1

Introduction

One of the central paradigms of modern technological advancement has been a steady reduction in the scale of things. Nanofabrication and imaging tools have developed to the point that controlling the dimensions of materials on length scales of tens of nanometers is routine in the manufacture of consumer devices. At the same time as the size of components has scaled down, the increased efficiency, reduction in cost, and improvement in quality has allowed the complexity of systems comprising them to scale up.

These advances are being paralleled by a revolution in the field of quantum science. Indeed, just as the tools have emerged to study and design material properties on nanometer length scales, so the opportunity to control the quantum nature of these devices continues to grow in importance. Specifically in the area of nanophotonics - devices that are shaped on lengthscales similar to the wavelength of optical light - the ability to design and control electromagnetic field modes so as to confine photons in wavelength-scale volumes promises to pave the way for scalable quantum networks - systems of individual quantum systems coherently interconnected via photonic links.

The first part of this thesis focuses on just such a quantum interconnect, based on Cavity Quantum Electrodynamics (CQED) with nitrogen vacancy (NV) centers in diamond. In this approach, an optical cavity provides tight confinement of a photon to the same location as a single, atom-like quantum emitter, as well as control over the spectrum of photonic modes in order to address the specific resonance frequency of the emitter. The result is a drastic alteration in the local electromagnetic environment of the emitter, causing a radical alteration of its relaxation dynamics. Chapters 2 and 3 describe two solutions to this problem based on photonic crystal cavities - periodically structured dielectric lattices that confine light via a photonic bandgap to a defect in the lattice structure.

At the other end of the nanophotonic device spectrum, structures that provide only weak confinement of light offer the opportunity to easily redirect photonic signals by coupling with high efficiency to the modes of a larger system. In this vein, we have engineered a broadband, high collection efficiency device based on a diamond nanobeam geometry to collect the emission from single NVs within the beam over a wide section of the NV phonon side band (PSB). The improved signal opens up new opportunities in quantum sensing and metrology, as well as new insights into the basic internal dynamics of the NV. In particular, we have demonstrated a mechanism to control the ionization dynamics of the NV based on its electron spin state. Chapter 4 describes this spin to charge conversion (SCC) mechanism and its application to enhanced sensitivity for AC magnetometry.

1.1 Nitrogen vacancy centers in diamond

The nitrogen vacancy color center in diamond is a solid state system with many atom-like properties of interest for quantum science. The NV is a defect in the diamond lattice consisting of a substitutional nitrogen next to a vacancy. The energy levels and transitions that are relevant to this thesis are show in Fig. 1.1. In particular, the NV exists in two charge state configurations, NV^- and NV^0, and can switch between the two through a photoionization process, the dynamics of which we study in detail in Chapter 4. The negatively charged configuration has an optical transition at 637 nm that can be stable and narrowband at low temperature[1]. It is this transition that is targeted for NV-cavity coupling, which we demonstrate in Chapters 2 and 3. The orbital ground and excited states are spin triplets, and the spin dynamics enable applications in nanoscale sensing. In particular, in the ground state the $|m_s = 0\rangle$ sublevel is separated from the $|m_s = \pm 1\rangle$ sublevels by the 2.8 GHz zero-field splitting due to electron dipole-dipole interactions. Application of an external magnetic field can futher separate the $|m_s = \pm 1\rangle$ from each other via Zeeman splitting. A microwave driving field between $|m_s = 0\rangle$ and $|m_s = 1\rangle$ constitutes an effective two-level system in the ground state.

An important feature of the NV center is a mechanism to polarize and read out the spin state optically. An inter-system crossing between the $|m_s = \pm 1\rangle$ levels in the excited state and a manifold of singlet states results in shelving of $|m_s = \pm 1\rangle$ population into a metastable singlet state. The relatively long lifetime of the singlet state (~ 150 ns at room temperature[2]) results in a fluorescence contrast between an initial $|m_s = 0\rangle$ and $|m_s = 1\rangle$ state when the NV pumped into the excited state. Additionally, the singlet state decays to $|m_s = 0\rangle$, so that by driving the NV with, for

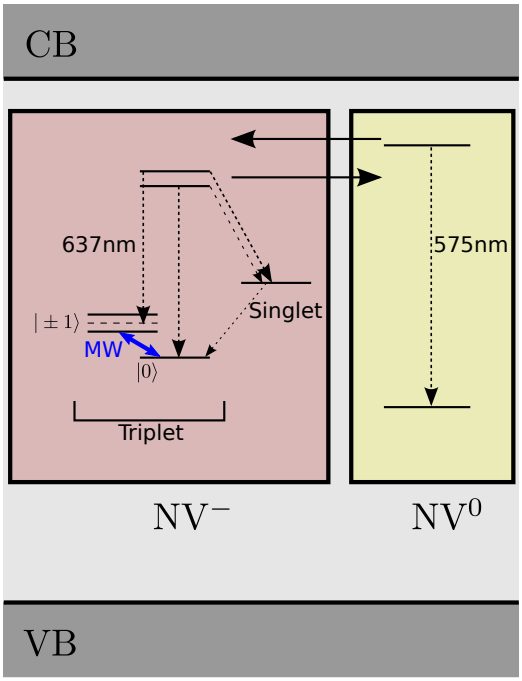

Figure 1.1: Level diagram for the NV center.

example, 532 nm laser light, the spin can be polarized into $|m_s = 0\rangle$.

1.2 Cavity Quantum Electrodynamics with NV centers in Photonic Crystals

In free space, an atom in its excited state will spontaneously decay and emit a photon into the continuum bath of modes forming its electromagnetic environment. This behavior changes dramatically when the atom is placed in a cavity, where the photonic environment is modified to strongly enhance the atom's coupling to a single optical mode, an effect first described by Purcell[3]. This effect has been studied for atoms in free space coupled to Fabry-Perot type cavities, giving rise to impressive demonstrations such as cavity Fock state preparation[4], single photon generation[5], and single-photon switching[6].

There has been substantial effort to translate these results to solid-state systems, where the emitter is embedded in a crystalline material and the cavity is a photonic crystal, microtoroid, or other chip based device. This is attractive for its potential scalability, as well as avoiding the difficulties inherent to trapping atoms in free space. From the point of view of basic CQED physics, though, nanoscale cavities offer the exciting prospect of wavelength scale mode volumes, resulting in very large emitter-cavity interaction strengths. The interaction strength is governed by the electric field energy density of the cavity mode, which is inversely proportional to mode volume, V. Therefore, by making the cavity mode as small as possible, large enhancements are possible even with relaxed requirements for cavity quality factor, Q. Typical mode volumes for photonic crystal cavities are $V \sim (\lambda/n)^3$, where λ is the wavelength in vacuum and n is the cavity refractive index. Thus, photonic crystal cavities have

much to offer for CQED applications.

Along these lines, many key results have been achieved for solid state CQED devices comprising quantum dots coupled to photonic crystals fabricated from the quantum dot host material[7,8,9]. There is substantial interest in extending these results to NV centers due to their long spin coherence time, which makes them attractive as quantum storage nodes.

Two major challenges make this task especially difficult for the NV relative to atoms in free space or quantum dots. The first is the NV's strong phonon sideband (PSB). Only that part of the spectrum within the cavity line will be enhanced, and in the case of the NV 95% of the emission is in the broad PSB, with only 5% concentrated in the narrow zero phonon line (ZPL). This makes the task of coherent NV-cavity coupling a factor of 20 harder than in the case of an atom in free space, where all of the fluorescence is concentrated in single, narrow transition line. For an NV with a transform-limited linewidth, reaching the Purcell regime - where the NV is more strongly coupled to the cavity than to other decay channels - requires an enhancement factor of 20, whereas the equivalent requirement for atoms in free-space is an enhancement factor of 1.

NV-cavity coupling in the Purcell regime has now been demonstrated[10], but in order to create useful quantum devices a second challenge must be overcome. Because of nearby defects and charge traps in the diamond, the NV ZPL shifts in frequency and is effectively broadened beyond the natural, transform-limited linewidth of $2\pi \times 15\,\mathrm{MHz}$. This so-called "spectral diffusion" limits the utility of any photonic enhancement for quantum applications. For instance, in the case of single photon generation, the enhancement factor required to source identical, transform limited photons would increase by the same factor as the linewidth broadening. To achieve this

for an NV with a relatively narrow low spectral diffusion linewidth of $2\pi \times 100\,\mathrm{MHz}$ would require cavity quality factors of $\sim 10^4$ and perfect spatial alignment of the NV to the cavity mode maximum, which is at the edge of current fabrication capabilities. In nanostructured diamond, however, the spectral diffusion is typically larger by a factor of 10, necessitating the development of materials processing techniques to reduce its influence. Nevertheless, significant progress continues to be made, both in cavity fabrication and in material processing, bringing quantum networks based on NV-cavity nodes ever closer to reality.

In this thesis, we have realized two approaches to CQED with NV centers, both of which employ photonic crystal cavities. The first is a hybrid approach where the NV is contained in a diamond nanocrystal and the photonic crystal is fabricated out of a GaP membrane, as described in Chapter 2. This approach was the first to demonstrate coupling between a single NV and a photonic crystal cavity, with a modest fluorescence enhancement factor of 7[11]. Similar work was reported around the same time by two groups[12,13]. The advantages of this approach are twofold. First, the spatial alignment between cavity and nanocrystal can be controlled at will using a piezo-controlled probe tip, which allowed us to not only optimize the spatial overlap but also to explore the spatial dependence of the coupling and map out the cavity mode. Second, fabrication procedures in GaP are relatively mature, allowing for fabrication of high Q devices.

Although the hybrid approach achieved rapid success, a major drawback is the difficulty in implementing this approach with bulk diamond samples, where the spectral diffusion issue is more tractable. Due to the high index of the bulk diamond ($n = 2.4$), it is difficult to maintain a high Q in the presence of an extended piece of diamond. Although there has been some success in this direction[14], the advent of

improved diamond fabrication procedures has eliminated the attraction of the hybrid approach, in favor of all-diamond architectures.

The second approach pursued here is exactly this sort of all-diamond architecture[15]. We fabricated photonic crystal cavities by thinning down a diamond sample to the device layer thickness and then transferring the photonic crystal pattern into the diamond film via a vertical reactive ion etch (RIE). We demonstrated tuning to the ZPL of the NV, observing an enhancement in ZPL counts by a factor of 7. Other groups have recently demonstrated NV coupling to 2D photonic crystal cavities[10] and ring resonators[16] fabricated from diamond with a similar process. This approach is described in Chapter 3.

Although much progress has been made, two main challenges stand out for NV center-photonic crystal cavity coupling going forward. First and foremost is the issue of spectral diffusion of the optical transition frequency in nanofabricated devices[10]. Although progress has been made in controlling spectral diffusion for NVs implanted into bulk samples[1], controlling spectral diffusion in nanofabricated samples remains a major challenge. A secondary challenge is the issue of deterministically implanting or otherwise preparing an NV in the cavity mode maximum. To date, all examples of NV-cavity coupling in monolithic diamond have relied on random alignment between the NV center and the cavity. In principle, methods for deterministic placement are possible, either by directly implanting the NV into the cavity mode[17], or by aligning the cavity to a predetermined NV. Active efforts to address these problems are under way in our group.

1.3 Nanoscale metrology

A major application for NV centers involves nanoscale metrology[18,19,20,21]. The electron spin sublevels are sensitive to magnetic and electric fields, and the capability to form stable NV centers within tens of nanometers of the diamond surface enables field sensing on nanoscopic length scales. Particularly in biological systems, where room temperature operation and inert, non-toxic materials are necessary for *in vivo* studies, NV centers have emerged as a promising system for sensing fields on length scales relevant to cellular processes. In this thesis we employ two techniques to enhance NV nanoscale metrology. First, we designed a nanophotonic device that yields a high photon collection efficiency, and second, we used it to study the internal NV charge dynamics and to develop a mechanism for converting the electron spin state into a charge state, to reduce spin readout noise.

As a concrete application, we consider the case of AC magnetometry, for which the sensitivity is dependent on two factors: the spin coherence time, and the noise associated with the spin readout process. Advances in material growth[22] and processing[23], as well as dynamical decoupling protocols[24,25,26], have extended the spin coherence time into the millisecond range. We demonstrate improvements to spin readout that directly translate into improved sensitivity for NV magnetometry.

Chapter 2

Deterministic Coupling of a Single NV Center to a Photonic Crystal Cavity

In this chapter, we describe and experimentally demonstrate a technique for deterministic, large coupling between a photonic crystal (PC) nanocavity and single photon emitters. The technique is based on in-situ scanning of the PC cavity over a sample, and allows the precise positioning of the cavity over a desired emitter with nanoscale resolution. The power of the technique is demonstrated by coupling the PC nanocavity to a single nitrogen vacancy (NV) center in diamond, an emitter system that provides optically accessible electron and nuclear spin qubits.

2.1 Introduction

Optical resonators enable large amplification of small optical signals, resulting in a range of spectroscopic and sensing applications, and have allowed for detection of single atoms[27], molecules[28], and quantum dots[9,29]. In addition, they enable a controllable coupling between optical emitters and the cavity vacuum field that is critical

for efficient light sources[30,31,32] and for the realization of memory nodes in quantum networks[33] and quantum repeaters[34]. This coupling strength scales with the cavity mode volume V_m as $1/\sqrt{V_m}$, and consequently, nanoscale photonic crystal (PC) cavities have been explored extensively in solid-state cavity QED applications. While much progress has been achieved in coupling quantum dots to PC cavities made from the host material[7,8,9], extending these techniques to fully deterministic coupling and to other material systems has been difficult. Specifically, there has been much recent interest in coupling PC resonators to NV centers[13,35,36,37], a promising single photon emitter with excellent electronic and nuclear spin memory[38,39,40], though experimental demonstrations have remained a challenge.

In this chapter, we demonstrate a technique for deterministic positioning of micron-scale PC slabs that support high quality factor (Q) cavity modes with nanometer-scale features. When such a cavity is scanned over the sample, it can be used for deterministic coupling to optically active systems with sub-wavelength resolution via the evanescent field. By appropriate design of PC cavities and waveguides, these systems combine sub-wavelength resolution, high throughput, and cavity-enhanced sensitivity. In particular, they can be deterministically interfaced with isolated optical emitters.

2.2 PC DESIGN, FABRICATION, AND CHARACTERIZATION

In our experiments, the PC consists of a triangular lattice of air holes in a gallium phosphide (GaP) membrane, creating an optical bandgap that confines light in the slab to a cavity region. The bandgap along the ΓX crystal direction is shown in the dispersion diagram in Figure 2.1(a). Confinement in the vertical direction occurs through total internal reflection (TIR) for modes with frequencies below the air light-

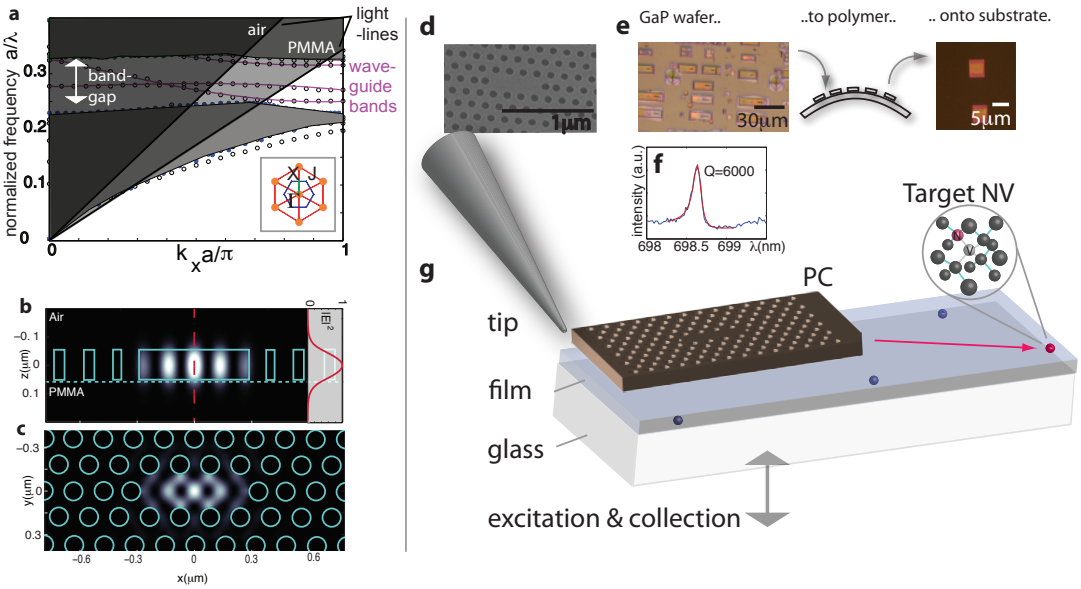

Figure 2.1: (a) Dispersion for the photonic crystal slab in air, along the waveguide direction k_x; the inset shows the crystal (orange) and inverse crystal (blue) directions. The lattice has a periodicity of $a = 176$nm, hole radius of $\sim 53\,\mathrm{nm}$, and slab height of $\sim 110\,\mathrm{nm}$. (b) Energy density for fundamental mode in cross-section and (c) in plane. (d) SEM. (e) The photonic crystals are transferred from the GaP chip onto a substrate via a polymer stamp. (f) Broad-band reflectivity measurement of a cavity resonance with $Q \approx 6 \cdot 10^3$. (g) The PC slab is positioned relative to a target nanocrystal in the polymer film.

line indicated in Figure 2.1(a). A row of missing holes supports band modes which form bound cavity states when terminated on two sides. We employ a three-hole defect cavity[41] whose geometry is optimized for use on a Poly(methyl methacrylate) (PMMA) substrate with a refractive index of $n_s \sim 1.5$ (see Appendix A). The TIR-confined region in k-space is smaller on top of the PMMA, as sketched in Figure 2.1(a), but simulations indicate that the Q value can still be above $13 \cdot 10^3$. The cavity has a mode volume $V_m = 0.74(\lambda/n_{\mathrm{GaP}})^3$, where $n_{\mathrm{GaP}} = 3.4$ is the refractive index of GaP at $\lambda = 670$nm. The fundamental mode of the PC cavity is depicted by its energy density in Figure 2.1(c). The cross section in Figure 2.1(b) shows the evanescent tail of the mode that couples to emitters.

We fabricate GaP PC nanocavities by a combination of electron beam lithography and dry etching[42] of a 108nm membrane of GaP on top of a 940nm-thick sacrificial layer of a $Al_{0.85}Ga_{0.15}P$. A wet etch removes the sacrificial layer, leaving free-standing photonic crystal membranes. The scanning electron micrograph (SEM) of a resulting PC nanocavity is shown in Figure 2.1(d). Reflectivity measurements of freestanding cavities indicate that quality factors (Q) of these cavities can exceed $6 \cdot 10^3$, the maximum value that can be measured with the resolution of our spectrometer (Figure 2.1(f)). However, in the remainder of this paper we will study cavities with typical Q values below 1000, since these were more reliably fabricated in large numbers, permitting systematic studies. To transfer cavities, we press the GaP chip against a flexible polymer layer of Polydimethylsiloxane (PDMS), which separates the PC membranes from the chip while preserving their arrangement. The adhesion between the membranes and the PDMS is weak enough so that the GaP structures can be stamped onto the sample that is to be imaged, as shown in Figure 2.1(e). In our demonstration, the sample consists of ~ 30 nm diamond nanocrystals that are dispersed on a

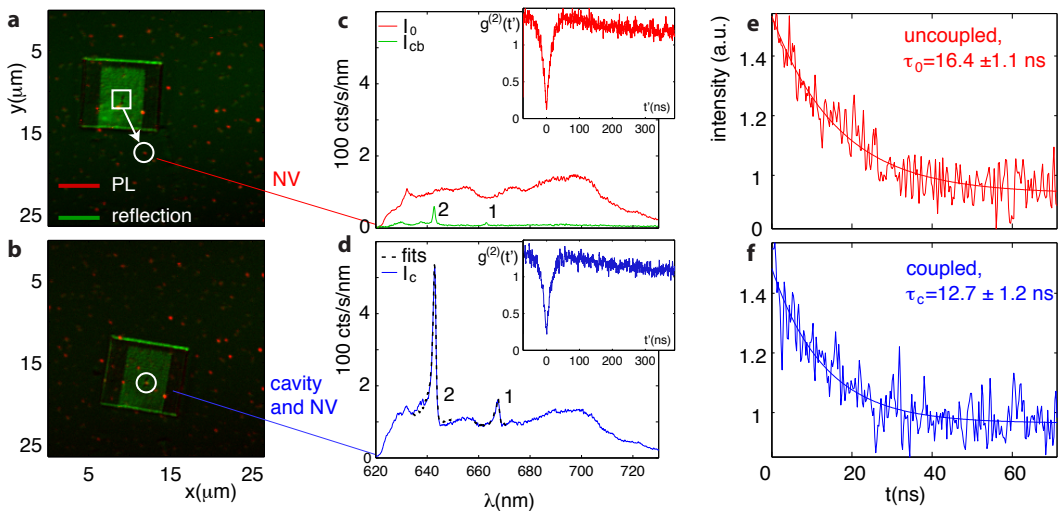

Figure 2.2: The photonic crystal is moved from an initial uncoupled position (a) into alignment with the target NV center (b). The pump laser reflectivity is shown in green and the photoluminescence in red; pump laser power is $500\,\mu\mathrm{W}$, focused to $\sim 0.2\,\mu\mathrm{m}$. (c) PL spectrum of the uncoupled NV (I_0) and uncoupled cavity background (I_{cb}). A photon correlation measurement (see Appendix A) shows that the NV emission is strongly antibunched (inset); this feature is surrounded by photon bunching due to shelving in a metastable state of the NV emitter[43]. (d) PL spectrum I_c of the coupled NV-cavity system, again strongly antibunched (inset). A fit to theory (Eq.2.1) gives the SE rate into the cavity normalized by the background emission rate, $f^c(\lambda_2) = 5.3, f^c(\lambda_1) = 0.7$. (e) Time-resolved emission for the uncoupled NV, far removed from the PC membrane, and (f) the coupled NV. The $6\,\mathrm{ps}$ excitation pulse was generated by a frequency-doubled $1064\,\mathrm{nm}$ laser at $20\,\mathrm{MHz}$ repetition rate.

glass slide covered by a 100nm thick layer of PMMA, for which the transfer process succeeds with $\sim 80\%$ probability for each membrane. The sample is mounted in a scanning confocal microscope with an oil immersion lens. A tungsten tip with $0.5\,\mu\mathrm{m}$ radius is used to scan and position a PC nanocavity with nanometer resolution (Figure 2.1(g)).

Figure 2.2(a) shows a room-temperature photoluminescence (PL) image of a typical sample (red signal) obtained by scanning a green excitation laser across the surface with galvanometric mirrors. The PL spots in the image correspond to single or clusters of NV centers in diamond nanocrystals. The PC nanocavity can be located with

the excitation laser reflection (green in Figure 2.2(a)) as well as weak fluorescence originating from impurities in GaP and PMMA (green curve in Figure 2.2(c)). The PC fluorescence clearly shows two resonances at $\lambda_1 = 667.3\,\text{nm}$ and $\lambda_2 = 643.0\,\text{nm}$ with quality factors $Q_1 = 550$ and $Q_2 = 610$. These quality factors are rather low because of variabilities in the fabrication; we saw no degradation due to the transfer onto the PMMA substrate. By collecting the spectrum at different points within the cavity (see Appendix A), we can identify peak 1 as the fundamental mode depicted in Figure 2.1(c) and peak 2 as two nearly degenerate, oppositely polarized higher-order modes of the cavity.

2.3 Deterministic coupling

We achieve deterministic coupling between the NV and the nanocavity by first selecting a 'target' NV (indicated in Figure 2.2(a)). This center exhibits a broad spectrum I_0 (Figure 2.2(c)), which is characteristic of NV centers and results from a broad phonon sideband extending from ~ 640 to $800\,\text{nm}$. Importantly, the emission exhibits a strongly anti-bunched autocorrelation (inset), indicating that it results from a single emitter. To couple this emitter to the cavity, we position the PC membrane over the target NV using the tungsten tip. As shown in Figure 2.2(d), the PL spectrum I_c changes dramatically and shows strong peaks on resonance with the cavity modes. The intensities of these peaks are far higher than the cavity background, I_{cb}. Moreover, the autocorrelation of the coupled NV-cavity system is again strongly anti-bunched (Figure 2.2(d)), indicating that it is driven by emission of the NV center. We also verified the electronic triplet state of the coupled NV by electron spin resonance (ESR) measurements (see Appendix A).

The SE rate of an NV center is also modified by the presence of the PC slab. Specifically, Figures 2.2(e) and (f) show that the lifetimes of the uncoupled and coupled NV centers are $\tau_{0,c} = 16.4 \pm 1.1, 12.7 \pm 1.5\,\mathrm{ns}$, respectively. The PL spectra on and off the PC coupled with lifetime measurements allow the determination of the spectrally resolved SE rate enhancement, $F(\lambda)$, of the coupled emitter via the relation $F(\lambda) = I_c(\lambda)\tau_0/I_0(\lambda)\tau_c$ (see Appendix A): the analysis of the data in 2 yields $F(\lambda_1) = 2.2$ and $F(\lambda_2) \sim 7.0$ (the full curve $F(\lambda)$ is plotted in Appendix A).

We next demonstrate the spatial resolution of our method. By monitoring the fluorescence spectrum while scanning the cavity over the NV, we can map out the near-field emitter-cavity coupling. This is demonstrated in Fig 3(a-e), where we scan the cavity along its longitudinal (x-axis) over the sample in 3.4 nm steps. Figure 3(f) presents a series of PL spectra acquired as the cavity moves over the emitter, and reveals an intensity oscillation with a period corresponding to one PC lattice spacing, $a \sim 180\,\mathrm{nm}$. This oscillation corresponds to the spatially dependent SE modification, which is directly proportional to the cavity's electric field intensity.

To analyze our observations, we note that the fluorescence of the coupled NV-cavity system is given by the emission directly from the NV, the emission through the cavity, and interference between the two:

$$S_d(\omega, \vec{r}) = C_{NV} + C_{cav} f^c(\vec{r})|L(\omega)|^2 + 2C_{int}\Re[e^{i\Delta\phi}\sqrt{f^c(\vec{r})}L(\omega)], \tag{2.1}$$

where C_{NV}, C_{cav}, and C_{int} determine the relative contributions of the NV, the cavity, and their interference, respectively, which depend on the collection geometry and coupling to the collection fiber. $L(\omega) = 1/(1 + i(\omega - \omega_c)/\kappa)$ gives the Lorentzian line shape of the cavity resonance at ω_c with linewidth $\kappa = \omega_c/2Q$, and $\Delta\phi$ accounts for

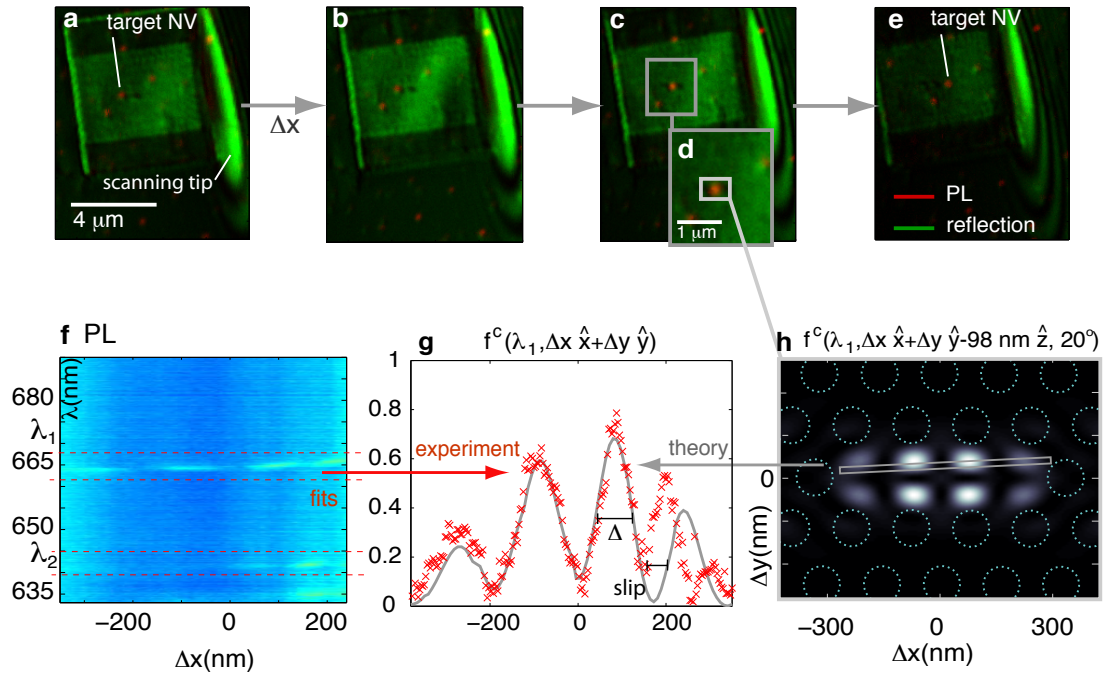

Figure 2.3: Scanning of the PC nanocavity probe in small steps, shown in snap-shots (a-e). (f) Photoluminescence scans for $\langle \Delta x \rangle = 3.4\,\mathrm{nm}$ average step sizes. (g) Fitted cavity SE rate enhancements $f^c(\lambda_1, \vec{r})$ for mode 1 showing a FWHM resolution of $\Delta \sim 80\,\mathrm{nm}$. (h) Expected SE enhancement factor $f^c(\lambda_1, \vec{r})$ and the estimated trajectory of the NV at $\Delta z = 98 \pm 5\,\mathrm{nm}$, $\Delta y = 70 \pm 5\,\mathrm{nm}$, and $\vec{\mu}$ in the plane at 20° to the x-axis. The indicated track matches the observed SE enhancement in (g).

the phase difference at the collection point between the direct NV emission and the emission through the cavity. The factor $f^c(\omega, \vec{r})$ is the SE rate enhancement of transitions in the phonon sideband of the NV with respect to the background emission rate into non-cavity modes.

The coefficients C_{NV}, C_{cav}, and C_{int} can be estimated from our experimental data as follows. Because of the high numerical aperture of our objective, nearly half of the emission from the cavity and the NV is collected: this observation suggests $C_{NV} \sim C_{cav}$. When the signal is collected through a single-mode fiber, the interference term represented by C_{int} becomes important and results in Fano-like features in the spectrum (see Appendix A)[44]. However, we find that the interference term vanishes when a multi-mode fiber is used, and we can set $C_{int} = 0$. A fit of Eq.2.1 to the spectrum in Figure 2.2(d) then yields $f^c(\lambda = 643\,\text{nm}, \vec{r}) = 5.3$, $f^c(667\,\text{nm}, \vec{r}) = 0.7$.

Since the signal in Figure 2.3(f) is proportional to $S_d(\omega, \vec{r})$, we can now use Eq.2.1 to compare the measured cavity signal to theory. Figure 2.3(g) plots the fitted values of $f^c(\omega_1, \vec{r})$ for the fundamental cavity mode frequency $\omega_1 = 2\pi c/\lambda_1$, as shown in the red crosses. By comparing the experimental $f^c(\omega_1, \vec{r})$ values to predictions for the cavity mode, we find a match between experiment and theory for an NV dipole μ that is $z = 98 \pm 5\,\text{nm}$ from the PC surface, as expected from the PMMA thickness, and at an angle of 20° to the x-axis, obtained from the best fit to the data. For these conditions, the predicted value of SE rate modification corresponds to the track graphed in Figure 2.3(h), in good agreement with experimental observations. A small discrepancy in the fit at $\Delta x \sim 190\,\text{nm}$ results primarily from positional slip of the PC cavity that can build up during the scan, a problem which could be improved by rigidly attaching the membrane to a stiffer scanning tip.

2.4 Conclusion

The high spatial resolution and frequency-selective modification of spontaneous emission opens new possibilities for efficient interfacing of promising solid state qubits via optical fields. For instance, while the NV center is a promising system for quantum information processing, only the emission occurring into the zero phonon line (ZPL) is suitable for coherent optical manipulation. The frequency-selective emission enhancement demonstrated here potentially allows us to direct most of the emission of the selected NV centers into the ZPL. Furthermore, the hybrid approach is compatible with narrow linewidth NV emitters in bulk diamond at low temperature. This opens the door for applications ranging from quantum repeaters to single photon nonlinear optics. Moreover, although we have focused here on NV centers, our scanning technique provides a 'cavity QED interface' that can be of use to a broad range of solid state qubits.

Furthermore, the PC scanning technique can serve as a new imaging approach, with sub-wavelength resolution and high throughput, which we term a scanning cavity microscope (SCM). Unlike other near-field probes that compromise the signal intensity to achieve high spatial resolution, SCM enables large count rates: in the demonstration shown here, we record up to $\sim 1 \cdot 10^6$ photons/s from a single NV, exceeding the collection with far field optics. This can be further improved by efficiently outcoupling through cavity-coupled waveguides. In addition, the spatial resolution of the SCM is determined by the feature size of the confined field, which is $\Delta \sim 80\,\mathrm{nm}$ for this cavity. This in-plane resolution may be improved substantially using cavity modes with small feature sizes, as in slot-waveguide cavities[45]. These qualities make the SCM a promising tool for label-free single molecule studies[28,46] or high-

resolution studies of local index variations in thin films[47,48]. Beyond high resolution and throughput, the SCM adds the capability to modify the spontaneous emission rate to near-field microscopy. This opens new possibilities for direct investigations of decay channels of optical emitters, such as light emitting diodes or fluorophores; for instance, by monitoring the emission intensity while effecting a known change in the radiative emission rate, the relative nonradiative recombation rate may be inferred, allowing a direct estimate of the radiative quantum efficiency of the material.

Chapter 3

Coupling of NV Centers to Photonic Crystal Nanobeams in Diamond

In this chapter we describe and demonstrate a technique for coupling single Nitrogen Vacancy (NV) centers to suspended diamond photonic crystal cavities with quality factors up to 6,000. Specifically, we present an enhancement of the NV center s zero-phonon line (ZPL) fluorescence by a factor of ~ 7 by tuning the cavity into resonance with the NV ZPL.

3.1 Introduction

The integration of solid state quantum emitters with sub-wavelength-scale optical devices has generated substantial interest in chip-based quantum networks[49]. Diamond is a particularly appealing platform for quantum photonics, as it is host to a number of different color centers[50], which can be individually integrated via ion implantation. Among them, the negatively charged NV center is an exceptional candidate for a quantum bit due to its spin readout and manipulation capabilities, which combined

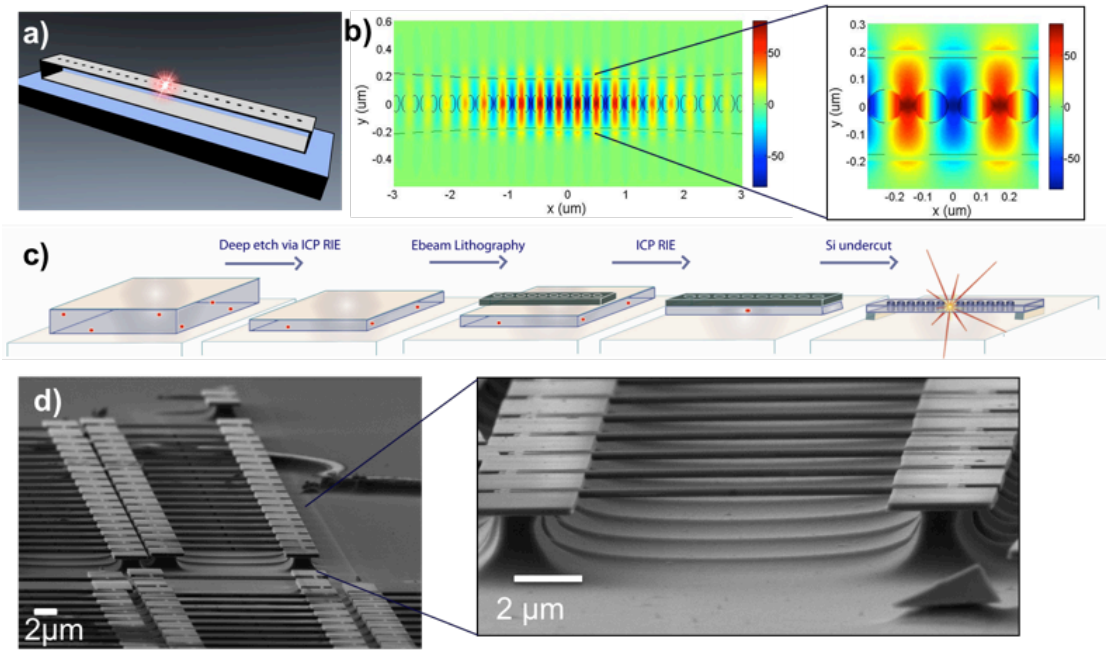

Figure 3.1: (a) Cartoon of a 1D photonic crystal nanobeam with an emitter coupled to the cavity. (b) FDTD modelling of the mode profile of a 1D photonic nanobeam. The hole diameter was constant while the width of the beam was tapered. (c) Fabrication schematic of diamond nanobeams: i) a diamond membrane was thinned to the optical device layer in a deep reactive ion etch; ii) next, EBL was performed to define the mask, and iii) the mask was transferred into the diamond via RIE. iv) Finally, the diamond nanobeams were undercut in an isotropic RIE step that removes underlying Si layer. (d) SEM image of freestanding diamond nanobeams.

with long coherence times can be leveraged for quantum information science[51,52,53,38], quantum sensing[19,20,54] and quantum networks[55,56]. These potential applications all either require or benefit from optimized collection efficiency as well as control of spectral and spatial properties of spontaneously emitted photons.

An appealing approach to addressing these problems involves the use of Cavity Quantum Electrodynamics (CQED). Here, the single photon spontaneous emission rate can be controlled by a photonic cavity that enhances the interaction strength between a single optical mode and the NV center. In the case of the NV center, these benefits can be realized by cavity coupling to the narrow-band zero-phonon line (ZPL)

transition, which constitutes 3-5% of photoluminescent emission (PLE) from the excited state. Indeed, many applications in quantum science rely on the interference between indistinguishable photons, for which only the ZPL transition is suitable. Coupling to an optical cavity thus provides a means to enhance both the ZPL collection efficiency and the relative proportion of photons emitted into the ZPL. In particular, photonic crystal cavities (PCCs), schematically depicted in Figure 3.1a, provide a strong enhancement due to their small mode volumes, and have been studied widely in the context of light-matter interactions with quantum dots[57,7].

To date, coupling between NV centers and PCCs has been demonstrated in several different systems that can be divided in two main categories: i) hybrid and ii) monolithic all-diamond approaches. Hybrid systems typically consist of cavities fabricated in non-diamond materials and are evanescently coupled to NV centers hosted in diamond nanocrystals. Examples include 2D PCCs cavities fabricated in GaP[58,59,60] and 1D plasmonic PCCs based on silver nanowires[61]. On the other hand, monolithic, all-diamond approaches are based on optical cavities fabricated directly in single crystal diamond substrates. Examples include microring resonators[16,62], 2D PCCs[10], and 1D PCCs[63,64]. While hybrid approaches can be straightforward to implement, they suffer from inferior quality of NV centers found in diamond nanocrystals, as well as reduced overlap between the cavity field and NV dipole. In this chapter, we demonstrate monolithic 1D PCCs fabricated from high purity single crystal diamond films with quality factors (Q) as high as 6000. We also demonstrate control of the cavity resonance using the combination of oxidation and diamond etching as well as inert-gas (Xe) deposition at low temperatures. Specifically, red tuning of the cavity resonance (up to 7 nm) is demonstrated by Xe deposition, and blue tuning of up to 23 nm was achieved by post-fabrication diamond etching. Using these techniques we were able to

bring the cavity mode into resonance with the NV center and demonstrate enhancement of the ZPL emission by a factor of 7 at low temperature.

3.2 PC design and fabrication from diamond membranes

To fabricate photonic crystals from a bulk piece of diamond, we employ a technique recently developed for diamond nanofabrication[16,62,10]. As depicted schematically in Figure 3.1c, we begin with a type IIa, <100> crystal oriented, CVD or Ib HPHT, single-crystal diamond membrane (Element Six) of $\sim 25\,\mu m$ thickness resting on a Si substrate. Next, we apply a deep reactive ion etch (RIE) in an oxygen inductively coupled plasma (ICP) to thin the membrane down to the desired device thickness of $\sim 250\,nm$. We then define an etch mask via e-beam lithography (EBL) on a hydrogen silsesquioxane (HSQ, Krayden) resist film spun on the diamond substrate. A second oxygen RIE step transfers the mask pattern into the diamond thin film. Finally, we remove the substrate material from beneath the devices with an isotropic etch recipe for Si in a RIE, resulting in suspended nanobeams. Figure 1d shows a scanning electron microscope (SEM) image of several photonic crystal nanobeams (left) as well as a magnified view (right).

Modelling of 1D nanobeams was performed using the 3D finite difference time domain (FDTD) software Lumerical. Our photonic crystals consist of a series of holes etched through a diamond ridge waveguide, illustrated schematically in Figure 3.1a. Light is confined to the waveguide by the index contrast between diamond ($n = 2.4$) and air, while the periodicity of the holes forms a bandgap to confine light along the waveguide. The particular parameters of our design were chosen to accommodate the inaccuracies of our fabrication process. In particular, devices obtained from the above

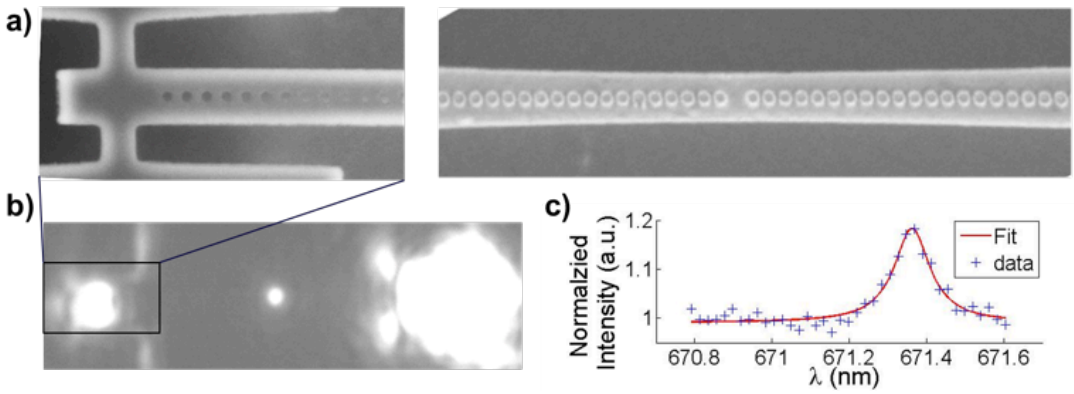

Figure 3.2: (a) SEM top view of a suspended photonic crystal nanobeam, (right) as well as of the outcoupling region for transmission measurements (left). (b) Transmission measurement obtained using white light from a supercontinuum source in-coupled at the right hand side of the waveguide. Out-coupled and up-scattered light is observed both at the cavity region as well as the other end of the cavity. The scattering of the cavity mode is well localized, indicating tight light localization in the small mode-volume optical cavity. (c) Spectra obtained at the cavity region in transmission show cavity modes with Q factors up to $\sim$ 6,000.

membrane-thinning procedure exhibit significant thickness variations from device to device across a single chip, owing to an initial thickness gradient in the mechanically polished diamond membrane, which is transferred to the film in the deep RIE step. As a result, we designed our photonic crystals to be robust to moderate variations in thickness within the range of 200-400 nm. To accomplish this, we used a relatively large hole radius (65 nm) and kept the hole radius and spacing uniform across the entire photonic crystal (we fabricated devices with hole spacing ranging from 165 nm to 175 nm). The cavity is then formed by tapering the width of the waveguide down from 500 nm at the ends to 400 nm at the cavity center, in a parabolic profile[65,66]. The quality (Q) factor for this cavity design is limited by coupling to the propagating waveguide mode, so that coupling between the nanobeam photonic crystal cavity and an optical waveguide can in principle be easily achieved[67]. This allows for integration of multiple devices on the same chip and realization of integrated quantum

networks. To achieve a high transmission signal ($T \propto Q_{Tot}^2/Q_{wg}^2$), the scattering Q factor ($Q_{scat} \approx 8 \cdot 10^6$) was designed much larger than the waveguide Q. The waveguide limited ($Q_{wg} \approx 5.3 \cdot 10^5$), total Q factor was determined to reach values up to $Q_{Tot} \approx 5 \cdot 10^5$, with a mode volume of $1.8 \cdot (\lambda/n)^3$, concentrated in the diamond (Figure 1b). Photons coupled into the optical waveguides were outcoupled at the end facet of the waveguide and collected using a lens with large numerical aperture (Figure 2a (left)). In addition, we explored an alternative cavity design with a central hole removed. This cavity geometry features a moderate, scattering limited Q factor ($Q_{scat} = 1 \cdot 10^4 < Q_{wg}$) and mode volume of $3.7(\lambda/n)^3$ and multimode behavior, but in turn increases the likelihood of locating an NV center within the cavity mode. A top-view SEM image of a suspended nanobeam showing the width taper and filled-in hole is presented in Figure 3.2a (right).

3.3 PC characterization

Characterization of the cavity spectral properties is performed in two ways. First, we probe the cavity response to a broadband input in a transmission configuration. We excite waveguide modes of the diamond nanobeam by coupling white light from a supercontinuum source (NKT Photonics) into the waveguide at one end. Light that is resonant will then couple to the cavity mode and, depending on the cavity design, either be scattered out from the cavity or transmitted to the far end of the waveguide and then outcoupled at the waveguide end. The balance between these two processes is determined by the ratio of scattering to waveguide-coupling Q factor. Figure 3.2b illustrates this behavior, with light focused onto the right end of the device and scattered from a well-localized spot at the cavity center and from the outcoupler at the

left end of the waveguide. We collect the scattered light from each location and analyze its spectrum to obtain the cavity resonance frequency and Q factor (Figure 3.2c). With this method we measured spectrometer-limited Q factors exceeding 6,000.

For devices containing an NV center, the cavity spectral properties can also be measured in the PLE spectrum of the NV center, as follows. The presence of an NV center in the vicinity of the cavity is determined by confocal microscopy. A 532 nm laser (Coherent Compass 315M) is focused onto the sample and scanned over the field of view to excite randomly positioned NV centers formed during the growth of the diamond. Photons emitted from an NV center are then collected (green light is filtered out) and NV centers are identified as bright spots (Figure 3.3a). Single NV centers were identified by measuring the second-order autocorrelation of the PLE signal, due to their characteristic antibunching dip (Figure 3.3b)[68]. The NV PLE contains components from both charge states (NV- and NV0), and the broad phonon sideband (PSB) provides a relatively flat, broadband source with which to probe the frequency of cavity modes over a range from 575-800 nm. The emission of the NV center coupled to the cavity thus exhibits intensity peaks at the cavity resonances on top of a broad fluorescent background (Figure 3.3c). This approach can also be used to infer both the cavity frequency and Q factor, and these values were found to be in good agreement with values obtained using the white light transmission measurements. To further study our NV-cavity model system, we investigated the effects that the cavity has on the ZPL emission of the NV.

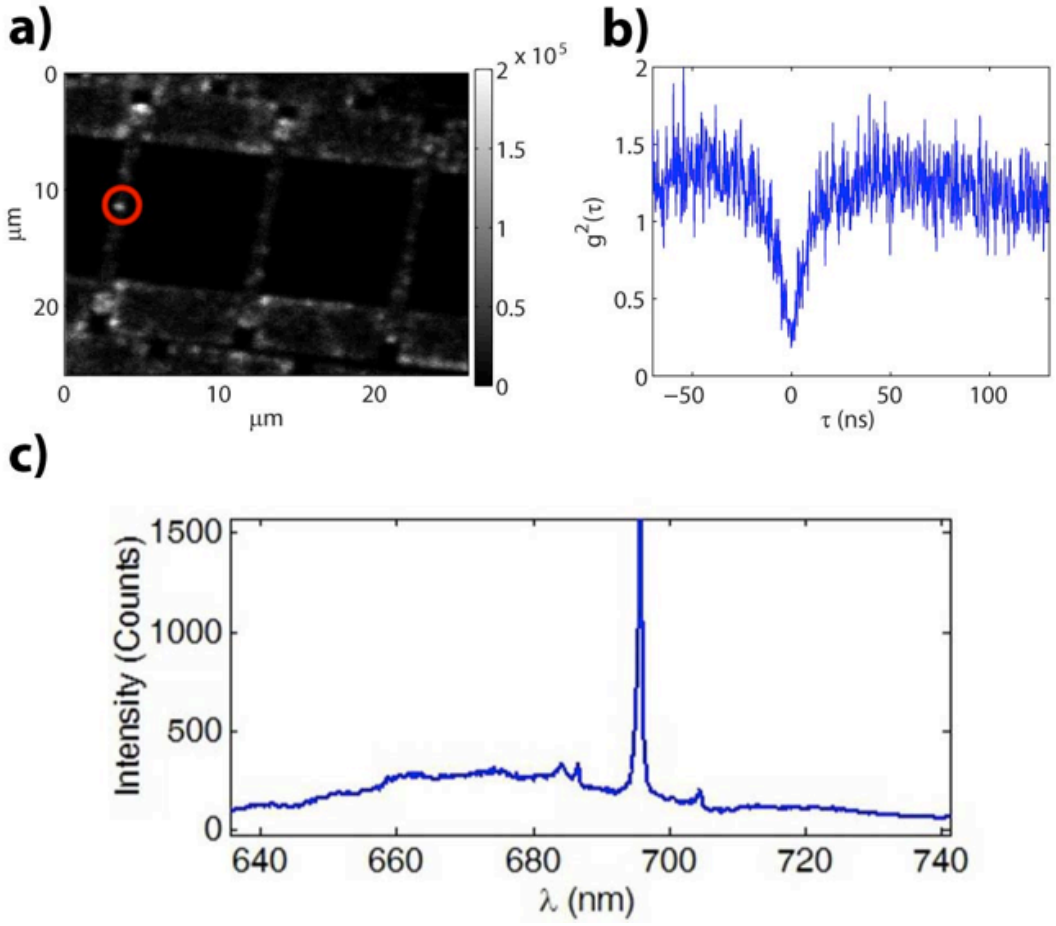

Figure 3.3: (a) Confocal microscope image of fluorescence from a device under excitation with $532\,\mathrm{nm}$ light. Individual NV centers are visible as bright spots along the nanobeam. (b) Second-order autocorrelation measurement of the fluorescence from an NV center in the cavity region of the nanobeam. The value for zero delay, $g^2(0) = 0.2$, is below 0.5, identifying it as a single NV center. (c) Fluorescence spectrum of the device collected directly from the NV center location. The broad phonon sideband of the NV center is coupled to the cavity at the resonance wavelengths ($685\,\mathrm{nm}$, $695\,\mathrm{nm}$, $705\,\mathrm{nm}$ and potentially $682\,\mathrm{nm}$) and the enhanced emission into the cavity is subsequently scattered into free space and collected by the objective along with the NV center emission.

3.4 Cavity spectral tuning

Integration of our cavities with NV centers for quantum optical applications requires spectral overlap with a narrow-band transition, associated with the ZPL. However, as discussed above, fabrication imperfections and diamond film wedging result in shifts of the cavity resonances from the predicted values, such that the cavity mode is, in general, not at the frequency of the ZPL transition. We employ two methods to tune our cavities, by either etching away material to blue-tune[63], or condensing Xe gas to red-tune[69]. The two techniques are complementary, the etching method working well for coarse, unidirectional tuning over a large range (up to $\sim 23\,\mathrm{nm}$), while the red-tuning method can tune in finer, reversible steps, but over a shorter range ($\sim 7\,\mathrm{nm}$). To take full advantage of these techniques we design our cavities to have resonances positioned to the red of the ZPL, so that an etching approach is then used to blue-tune cavities towards the ZPL and bring their resonances within the range of the Xe condensation technique. The latter is then used to achieve precise, in-situ tuning of the cavity and to bring it in resonance with the ZPL frequency.

The blue-tuning was achieved using two etching methods: i) an oxygen plasma etcher (Technics, Model 220), and ii) a rapid thermal annealing in oxygen environment (Modular Process Technology, RTP-600xp). The effect of these techniques on the cavity resonance frequency was studied over a series of etch steps of varying duration on a number of different cavities. The results are summarized in Figure 3.4 for a representative cavity with modest Q factor of ~ 1100. By varying the duration of the etch, we were able to tune the resonance in steps ranging from $0.2\,\mathrm{nm}$ to $5.3\,\mathrm{nm}$. We also note that the plasma etching approach has more reproducible etch rates than the oxidation approach. In total, we were able to tune by $\sim 23\,\mathrm{nm}$ over the course of

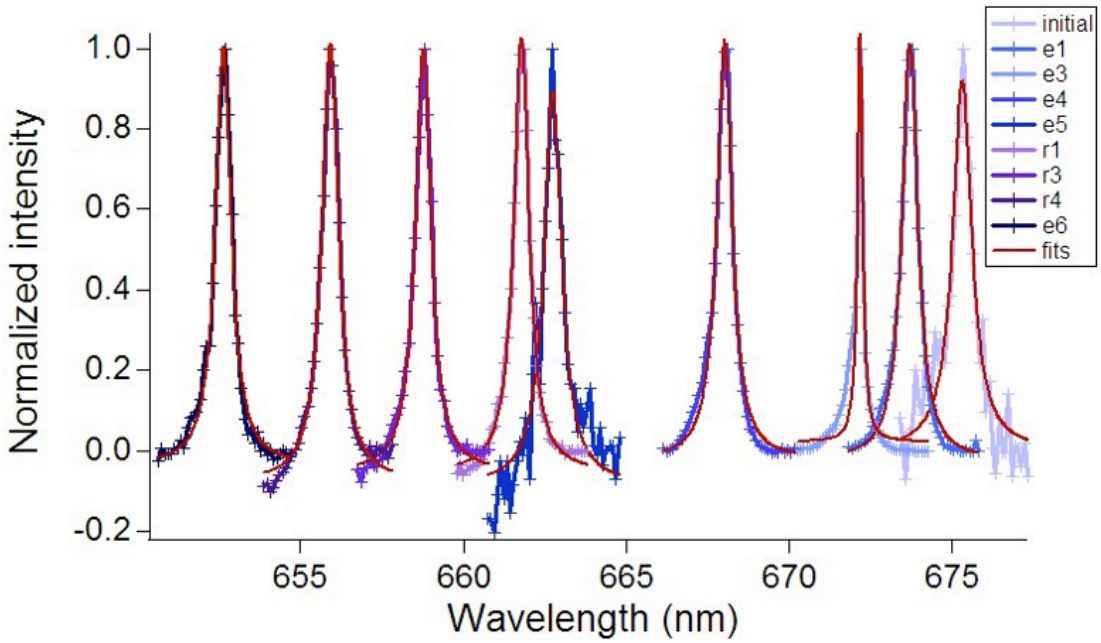

Figure 3.4: Controlled blue-tuning of a cavity mode via oxygen etching shown over 8 etching steps. "e" refers to etching in an oxygen plasma etcher, while "r" refers to etch steps performed by annealing the samples in oxygen atmosphere in a rapid thermal processor. The etch times are of differing lengths, background has been subtracted and modes are normalized by the peak intensity. An overall average tuning range of $\sim 23\,\mathrm{nm}$ was observed from several devices.

8 etch steps without deterioration of the Q factor.

3.5 Purcell enhancement of NV ZPL

Once the cavity resonance was tuned within range of the NV ZPL, the cavities were placed in a helium flow cryostat (Janis, ST-500) and cooled down to 4K. The spectrum of a representative device is shown as the bottom trace in Figure 3.5a (zoom in to the ZPL shown in Figure 3.5b). It can be seen that the emission spectrum features five distinct peaks: the 573 nm peak corresponds to diamond Raman line, the $\sim$ 613 nm, $\sim$ 622 nm and $\sim$ 631 nm peaks correspond to three cavity resonances, while the 637 nm peak is associated with the NV center ZPL. We note that this particular NV exhibits a ZPL split into two different resonances (Figure 5b), which we attribute to strain-induced drifts in the ZPL frequency. Next, Xe gas was introduced into the cryostat through a nozzle directed at the sample and positioned $\sim$ 1 cm away from it. Spectra were then collected for successive depositions of Xe onto the cavity (Figures 3.5a and 3.5b). The diamond Raman line and NV ZPL are fixed and do not shift in frequency with the introduction of additional Xe, while the three cavity resonances red-shift with increasing deposition. We note that the cavity tuning was observed within seconds of the Xe being released, after which the cavity frequencies remain stable for hours, indicating no further gas dynamics. Reheating the sample to room temperature reverses the tuning. With this procedure we were able to repeatedly tune over a range of $\sim$ 7 nm in step sizes of $\sim$ 0.5 nm, without significant degradation of the cavity Q.

As the cavity is tuned into resonance with the ZPL of the NV center, the total signal in the ZPL band is enhanced due to the interaction with the cavity mode. This

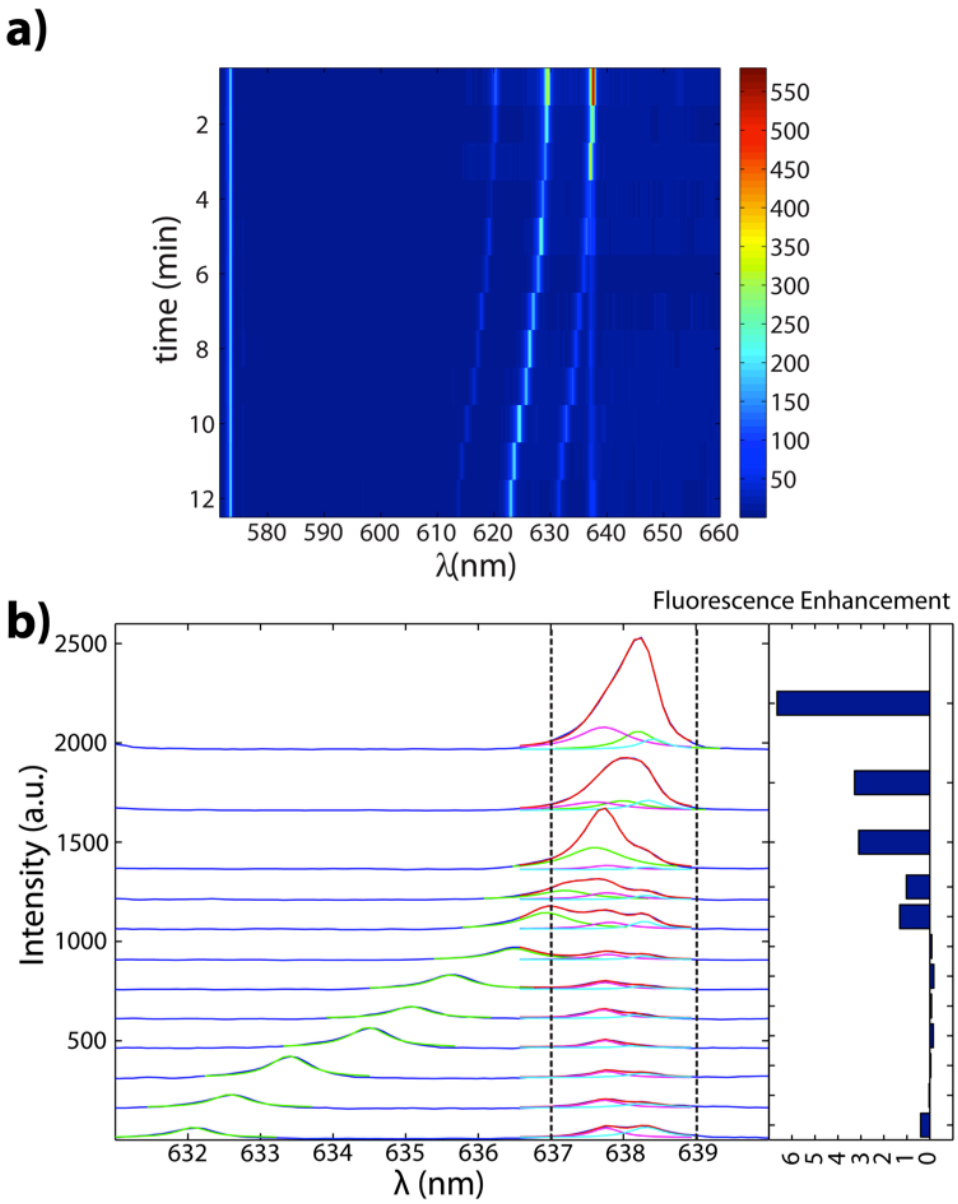

Figure 3.5: (a) Tuning the cavity into resonance with the ZPL of the NV center. The cavity is tuned into resonance by condensing Xe gas onto the device while continuously measuring spectra of the NV center at 4K in a cryostat. Xe is injected into the chamber where it condenses and red-shifts the resonance frequency of the cavity mode. When the cavity frequency overlaps the ZPL the fluorescence intensity is enhanced by a factor of $F_P \approx 7$. (b) Magnified and fitted version of (a), where a split ZPL is observed. The dashed lines indicate the limits for integration when estimating the Purcell factor. The histogram at the right represents the corresponding enhancement.

enhancement is induced by a combination of collection efficiency and Purcell enhancement for the part of the dipole fluorescence that is coupled to the cavity mode. In the case of a resonant interaction, the latter is given by:

$$F_P = \frac{3}{4\pi^2}\left(\frac{\lambda}{n}\right)^3 \frac{Q}{V}\frac{|\vec{E}_{NV}\cdot\vec{\mu}_{NV}|^2}{|\vec{E}_{max}|^2|\vec{\mu}_{NV}|^2}, \tag{3.1}$$

where $\vec{E}_{NV,max}$ are the cavity electric field at the position of the NV and cavity mode maximum, respectively, $\vec{\mu}_{NV}$ is the NV center dipole moment, λ is the vacuum wavelength of the cavity mode, $n = 2.4$ is the refractive index of diamond, and $V = \left[\int \epsilon(\vec{r})|\vec{E}(\vec{r})|^2 d\vec{r}\right] / \max\left[\epsilon(\vec{r})|\vec{E}(\vec{r})|^2\right]$ is the cavity mode volume.

Figure 5 shows the PLE spectrum through a series of Xe deposition steps, clearly indicating an enhancement of the ZPL intensity when the cavity comes into resonance. The spectra in Figure 3.5 have been normalized to the diamond Raman line at 573 nm to account for overall intensity fluctuations resulting from the Xe condensation.

By comparing the spectrum when the cavity is resonant with the ZPL to that when it is detuned, we can obtain an estimate of the fluorescence enhancement. In the case of a resonant cavity (as in the top spectrum of Figure 3.5), the total ZPL intensity is given by:

$$I_{ZPL}^{res} = (\eta_{cav}F_P + \eta_{NV})\frac{1}{\tau_0}, \tag{3.2}$$

where $\eta_{cav,NV}$ are the overall collection efficiencies for photons emitted by the cavity mode and directly by the NV center, respectively, and τ_0 is the NV center excited state lifetime in the absence of any Purcell enhancement. In the off-resonant case,

$F_P = 0$, so that:

$$I_{ZPL}^{off-res} = \frac{\eta_{NV} F_{NV}}{\tau_0}. \tag{3.3}$$

Dividing (3.2) by (3.3) and further making the assumption that $\eta_{cav} = \eta_{NV}$ (i.e. that the cavity Q is scattering-limited), we arrive at:

$$\chi = \frac{\eta_{cav} F_P}{\eta_N V} = \frac{I_{ZPL}^{res}}{I_{ZPL}^{off-res}} - 1. \tag{3.4}$$

The enhancement factor, χ, is shown in the right-hand panel of Figure 3.5b. A maximum fluorescence enhancement of 7 is observed when the cavity is resonant with the ZPL.

3.6 Conclusion and outlook

We expect that this modest enhancement can be substantially improved upon given the parameters measured for the present cavity. With a Q factor of 1634 and mode volume of $3.7 \cdot (\lambda/n)^3$, we expect an enhancement of 34 for ideal NV center placement and orientation. This discrepancy relative to our measured enhancement suggests further gains are possible by a more deterministic method for spatial alignment of the NV center with the cavity, in addition to improving the cavity Q factor through better fabrication.

In this work we have described the design and fabrication of suspended, 1D photonic crystal cavities made from high-purity, single-crystal diamond, and having Q factors of up to 6,000. Methods for blue tuning over a range of 23 nm and red tuning over a range of 7 nm were demonstrated, culminating in the selective enhancement of the ZPL intensity of a single NV center by a factor of 7, as verified by tuning a cav-

ity mode into resonance with the NV center's ZPL at low temperature. To facilitate the process of finding a device with a well-coupled NV center we used our lower-Q, higher mode volume design, however with our best fabricated cavities and an optimally placed NV center, we would expect an enhancement of up to 250. With smaller mode volume designs, more refined fabrication techniques to reduce side-wall roughness, and by developing deterministic methods for spatial alignment of the NV center within the cavity mode, even larger enhancement factors can be expected. Along with the recent work in 2D photonic crystals[10], these results open up promising avenues for new technologies in quantum sensing, quantum information science, and quantum networks[49].

The small 1D footprint and fabrication by RIE make the current approach scalable, with $\sim 10^3$ devices fabricated in parallel on a single chip. Additionally, the coupling to propagating waveguide modes, which occurs naturally in 1D photonic crystal devices, makes this geometry attractive for quantum networks and quantum information applications. Although improved methods must be found which allow for incorporation of these devices with implanted, stable NV centers, our method provides the framework for realizing such advanced quantum technologies.

Chapter 4

Spin to Charge Conversion in NV Centers

4.1 Introduction

The nitrogen vacancy (NV) center in diamond has attracted considerable interest as a solid state spin system with exceptional coherence properties, making it attractive for applications such as nanoscale magnetic, electric, and thermal sensing, and room temperature quantum computing. The key enabling properties common to these applications are a long electron spin coherence time and the ability to prepare and read out the spin state optically. For the NV, these properties exist in the negatively charged state (NV^-), and consequently NV^- has been heavily studied and analyzed. Additionally, the NV can exist in a neutrally charged state (NV^0), which plays a potentially important role in the system dynamics. Recently there has been increasing interest in the so-called "dark-state"[70,71] of the NV, which has been established to be NV^0[72,73]. Photoionization between the two charge states has been observed under

various illumination conditions[74]. However, previous studies of the charge state dynamics have focused on timescales that are much longer than the internal dynamics of the NV^- energy levels. Here we demonstrate that the ionization process from NV^- to NV^0 is spin dependent, such that the spin state of NV^- can be efficiently converted into a charge state, and we show that this spin to charge conversion (SCC) mechanism can be used for improved magnetic field sensing.

Here we demonstrate a new method for reading out the NV spin state that results from the SCC process, whereby $|m_s = 0\rangle$ is preferentially ionized to NV^0. Whereas the fluorescence contrast in the traditional readout scheme is limited by the relatively short lifetime of the singlet state (150ns at room temperature[2]), fluorescence contrast between the NV^0 and NV^- charge states can be quite high, allowing for single-shot charge state readout[74]. Consequently, the spin readout noise in the SCC readout process is not limited by photon shot noise, but rather by SCC efficiency. We find that the SCC limit on spin readout noise in our system is 2.76 times the spin projection noise level.

4.2 Experimental System

For our measurements we use naturally occurring NVs in type IIa chemical vapor deposition (CVD) grown diamond (Element6, 1 ppm N concentration). To enhance the photon collection efficiency, we carve the diamond into 300 nm wide beams and transfer them onto a glass coverslip for imaging with an oil-immersion confocal microscope (Fig. 4.1a). The nanobeams are fabricated with an angled Reactive Ion Etching (RIE) technique[64] that results in triangular cross-section waveguides with a width of 300 nm and a length of 20 µm, suspended above the diamond substrate by weak at-

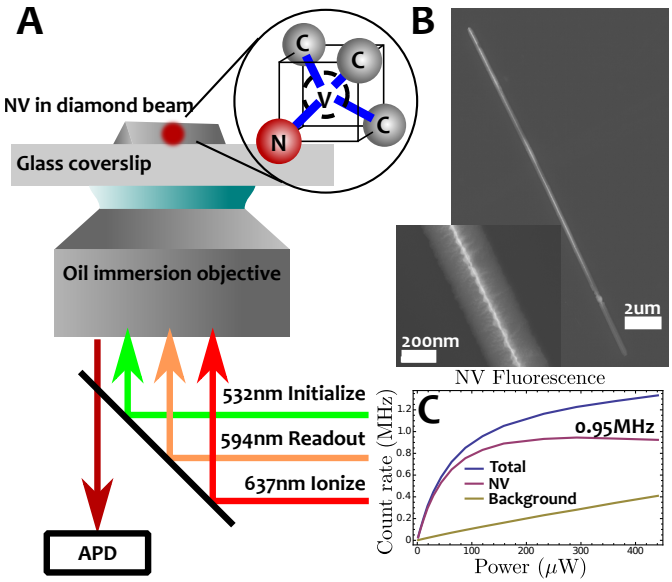

Figure 4.1: (a) We use an oil-immersion confocal microscope to illuminate and collect fluorescence from our NVs. AOMs control pulses of laser light at $532\,\mathrm{nm}$, $594\,\mathrm{nm}$, or $637\,\mathrm{nm}$ to control and measure the charge state of the NV. Fluorescence is imaged onto a multimode fiber and routed to an APD for photon counting. (b) The NVs are naturally occuring in type IIa diamond which we carve into triangular cross-section nanobeams (width=$310\,\mathrm{nm}$) and transfer to a glass coverslip for imaging. (c) Saturation fluorescence measurement for an NV in a diamond nanobeam. The maximum count rate under cw $532\,\mathrm{nm}$ illumination is 0.945 Mcps after background subtraction.

tachment points. Using a 500 nm radius tungsten STM probe tip mounted on a 3-axis piezo stage, we sever the suspended beams from the bulk diamond, pick them up via contact forces, place them on the glass coverslip, and orient them in a "face-down" position such that the smooth, unetched surface of the diamond is in contact with the glass (Fig. 4.1b).

To address the NV optically, we illuminate through a microscope objective (NA=1.49) with laser light at 532 nm, 594 nm, and 637 nm wavelengths, which serve to pump the charge state into NV^-, measure the charge state, and ionize from NV^- to NV^0, respectively. The timing and intensity of each laser is control by an acousto optic modulator (AOM). We collect photoluminescence (PL) from the NV through the same objective and image it onto a multimode fiber (core diameter = 62.5 µm). Because the width of the nanobeams is comparable to the wavelength of the NV emission, their photonic properties differ significantly from the case of bulk diamond, where the high index ($n_{diamond}$=2.4) results in most of the NV fluorescence being trapped inside the diamond due to total internal fluorescence. In particular, the effective refractive index of the waveguide mode can be made comparable to the index of glass (n_{glass}=1.5), so that the NV fluorescence is efficiently coupled to radiative modes in the glass. In this way we observe a maximum count rate of 0.945 million counts per second (cps) under cw 532 nm illumination (Fig. 4.1c).

For control of the NV^- electron spin sublevels, we align the magnetic field from a permanent magnet with the NV axis to split $|m_s = \pm 1\rangle$, and we place a copper wire (25 µm diameter) on the coverslip next to the beams, which delivers a microwave field to drive transitions between $|m_s = 0\rangle$ and $|m_s = 1\rangle$.

4.3 Measuring the Charge State

Central to our spin readout process is a mechanism for high-fidelity measurement of the NV charge state[74] that takes advantage of the fact that NV^- and NV^0 have different excitation and emission spectra, allowing for efficient spectral discrimination. To make a charge state measurement, we illuminate the NV with a low power of 594 nm light, which is near the maximum of the NV^- absorption sideband, but less energetic than the NV^0 zero phonon line (ZPL), so that NV^- fluoresces but NV^0 is mostly dark (Fig. 4.2a). Furthermore, we insert a 655 nm longpass filter in the collection path to eliminate any residual NV^0 fluorescence. In this way, we observe the NV^- count rate to be 20-30 times the NV^0 count rate (depending on illumination intensity, see Appendix B), resulting in a high contrast measurement (Fig. 4.2b).

The 594 nm light can also cause the NV to jump between charge states.[74] The NV first absorbs one photon and then, while in an excited configuration, absorbs a second photon, either exciting an electron to the conduction band to ionize NV^- to NV^0, or recapturing an electron from the valence band to convert NV^0 to NV^-. Thus, at low power, the ionization and recapture rates, g_1 and g_0, respectively, obey a quadratic power dependence, whereas the NV^0 and NV^- photon count rates, γ_0 and γ_1, respectively, obey a linear power dependence.[74] Consequently, the illumination power and integration time of the measurement can be adjusted to allow faster readout at the expense of lower readout fidelity.

4.3.1 Readout Fidelity vs. Measurement Time

To characterize the charge state readout fidelity, $\mathcal{F}_C$, of our setup, we measure the four rates, $g_{0,1}$, $\gamma_{0,1}$, under cw 594 nm illumination at a range of powers from 0.875 µW

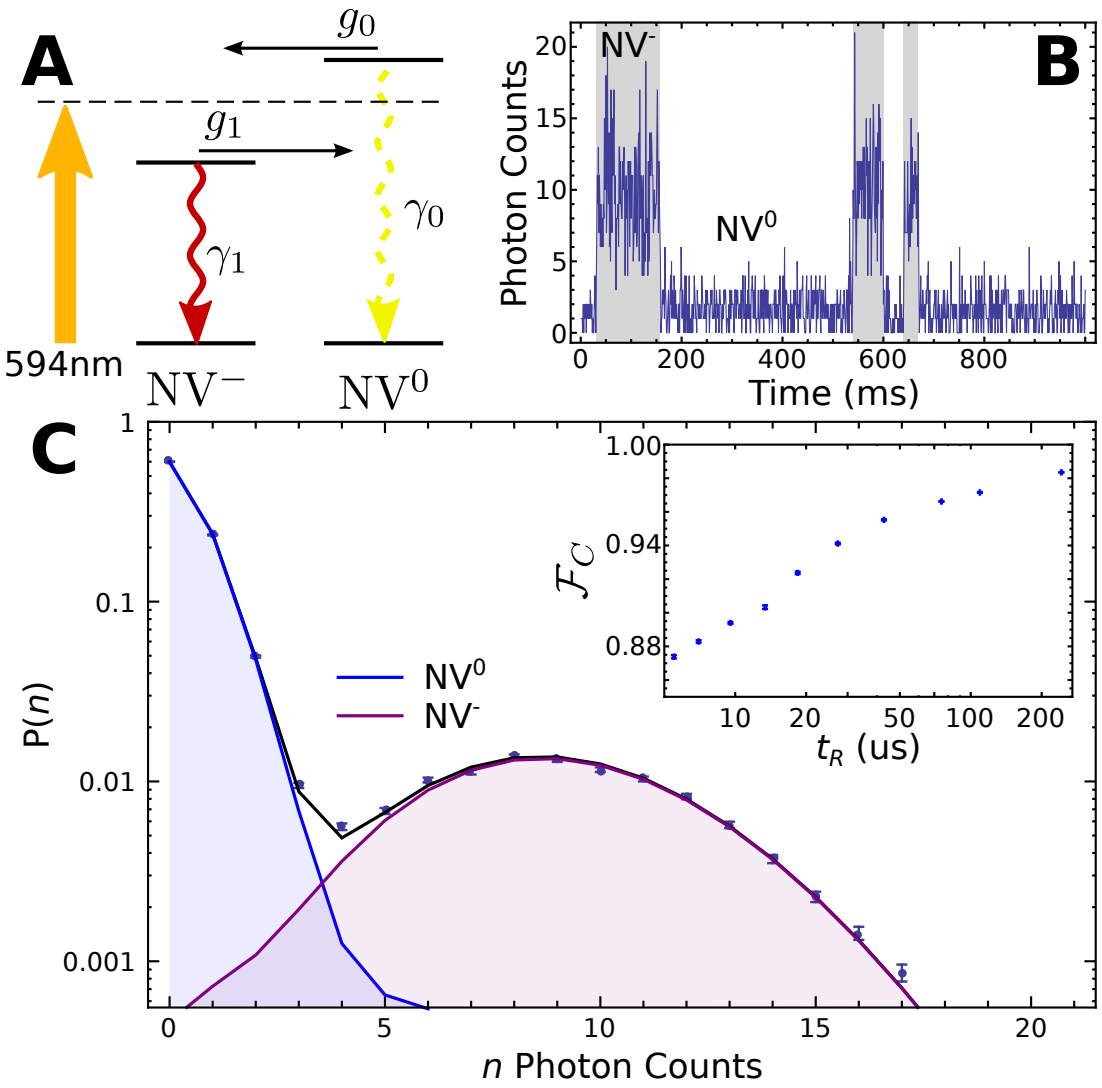

Figure 4.2: (a) Level diagram for the charge state readout process. $594\,\mathrm{nm}$ light excites NV$^-$ at the maximum of its absorption band, while NV^0 is only weakly excited, resulting in photon count rates γ_1, γ_0, respectively. Ionization occurs from the excited states of each charge configuration at rates g_1, g_0. (b) Time trace of fluorescence taken under cw $594\,\mathrm{nm}$ illumination at 410nW, showing jumps between NV^0 and NV$^-$. Counts were integrated for 1ms at each time point. (c) Photon number distribution for 100,000 measurements under cw $594\,\mathrm{nm}$ illumination at 820nW. Each measurement corresponds to 240μs integration time. The four rates $(\gamma_0, \gamma_1, g_0, g_1)$ are determined from a fit of the photon number distribution at each $594\,\mathrm{nm}$ power setting (see supplemental information). The charge state readout fidelity is calculated from the measured rates (inset).

to 15 µW. At each power, we record the number of photons detected in a time window, t, chosen so that $tg_1 \sim 1$ (in order that the resulting photon number statistics contain sufficient information to determine the ionization rates). We then fit the photon number distribution for 100,000 time windows with a model for the charge state dynamics to obtain the four rates at each power (see Supplementary Information for details). Once the rates are known for a given power, P, we calculate the optimal readout time, t_R, to maximize $\mathcal{F}_C(P)$ (Fig. 4.2c). We obtain reasonable fidelity ($\mathcal{F}_C \sim 0.9$) even for readout times as short as 10μs.

4.3.2 Charge Initialization

A similar measurement scheme can be used to rapidly initialize the NV into NV^-, such that the charge state is known to be NV^- whenever the initialization measurement succeeds. Whereas the above procedure achieves optimal readout fidelity for both NV^0 and NV^-, initialization requires only to verify that the charge state is NV^-. If verification fails, the procedure is repeated. To quickly initialize into NV^- with high fidelity, we first apply with a short, high power pump pulse of 532 nm light (150 ns at 300 µW) and then measure with a short probe pulse of 594 nm light ($t_{\text{probe}} =$ 900 ns at 11 µW) (Fig.4.3a). In this regime, $g_1 t_{\text{probe}} \ll 1$, so that ionization events are unlikely and a result of 1 or more photons is an accurate indicator that the final charge state is NV^-.

To verify our initialization fidelity, we performed a pump-probe combination followed by an optimal charge state readout at low power ($t_R = 240$ µs at 820 nW). In Fig. 4.3b,c, the photon number distribution for 100,000 measurements is shown, regardless of probe outcome (Fig. 4.3b, initialization fidelity 0.723 ± 0.006) and conditioned on the detection of one or more probe photons (Fig. 4.3c, initialization fidelity

0.975 ± 0.007). For these pump-probe conditions, a single initialization step "succeeds" (detects one or more probe photons) with probability $p_s = 0.216 \pm 0.001$.

4.4 Spin To Charge Conversion

We next show the ability to control the ionization dynamics in a spin dependent way, allowing for efficient conversion of the NV^- electron spin state to a charge state distribution. The mechanism for spin to charge conversion (SCC) is related to the well-established technique for optically detected magnetic resonance (ODMR)[75], in that it takes advantage of the spin-dependent shelving process to the metastable singlet state. From the singlet state, the NV cannot be excited to the triplet excited state, so the ionization process is blocked, resulting in a spin-dependent ionization process.

The SCC sequence is illustrated in Fig. 4.4a. We first initialize into NV^- and prepare the spin into either $|m_s = 1\rangle$ or $|m_s = 0\rangle$ (Fig. 4.4a(i)). We then apply a short, high power "shelving" pulse of 594 nm light, which either rapidly transfers the NV into the metastable singlet state in the case of $|m_s = 1\rangle$, or leaves it in the triplet manifold in the case of $|m_s = 0\rangle$ (Fig. 4.4a(ii)). Immediately following the shelving pulse, we apply a short, high power ionization pulse of 637 nm light, which ionizes the NV from the NV^- triplet manifold to NV^0, but does not ionize from the NV^- singlet state (Fig. 4.4a(iii)). Finally, we measure the charge state of the NV (Fig. 4.4a(iii)).

The resulting photon number distributions for this measurement are shown in Fig. 4.4b for an initial spin state of $|m_s = 0\rangle$ (top) and $|m_s = 1\rangle$ (bottom). The SCC parameters were 60 ns, 145 µW for the 594 nm shelving pulse and 20 ns, 22.5 mW for the 637 nm ionization pulse. The initialization sequence for this measurement consisted of a 40 ns, 300 µW pump pulse and a 500 µs, 500 nW probe pulse. The charge readout

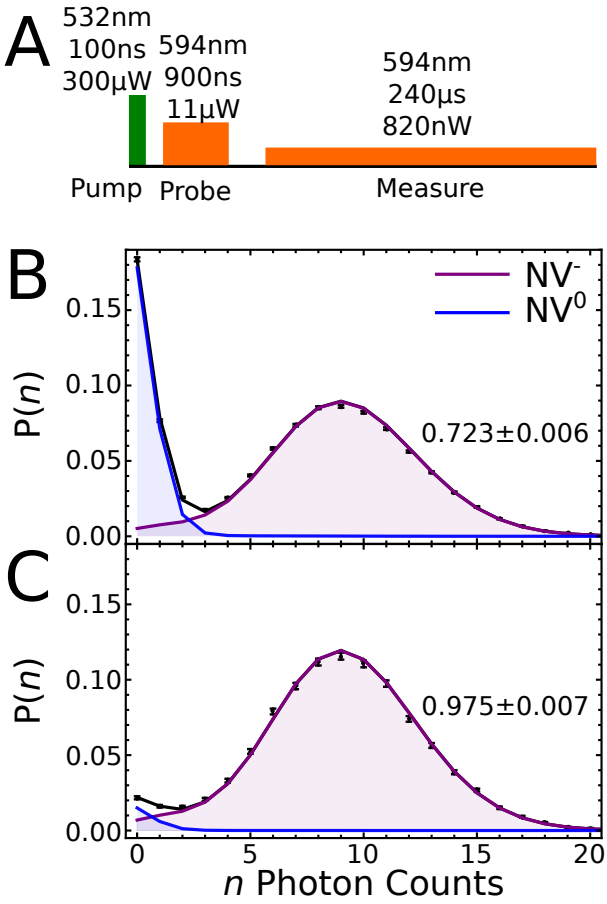

Figure 4.3: (a) Pulse sequence for charge state initialization. A $100\,\mathrm{ns}$ $532\,\mathrm{nm}$ pulse at $300\,\mu\mathrm{W}$ pumps the NV into NV^-, followed by a $900\,\mathrm{ns}$ $594\,\mathrm{nm}$ pulse at $11\,\mu\mathrm{W}$ that probes the charge state, and finally a $240\,\mu\mathrm{s}$ $594\,\mathrm{nm}$ pulse at $820\,\mathrm{nW}$ verifies the initialization. (b) Distribution of integrated photon counts during verification for 100,000 initialization measurements, regardless of probe outcome, indicating that the NV is pumped into NV^- with probability 0.723 ± 0.006. (c) Distribution for 100,000 measurements, conditioned on the presence of one or more photons during the $900\,\mathrm{ns}$ probe pulse. The probability of succeeding at the probe step is $p_s = 0.216 \pm 0.001$, and the NV^- initialization fidelity is 0.975±0.007.

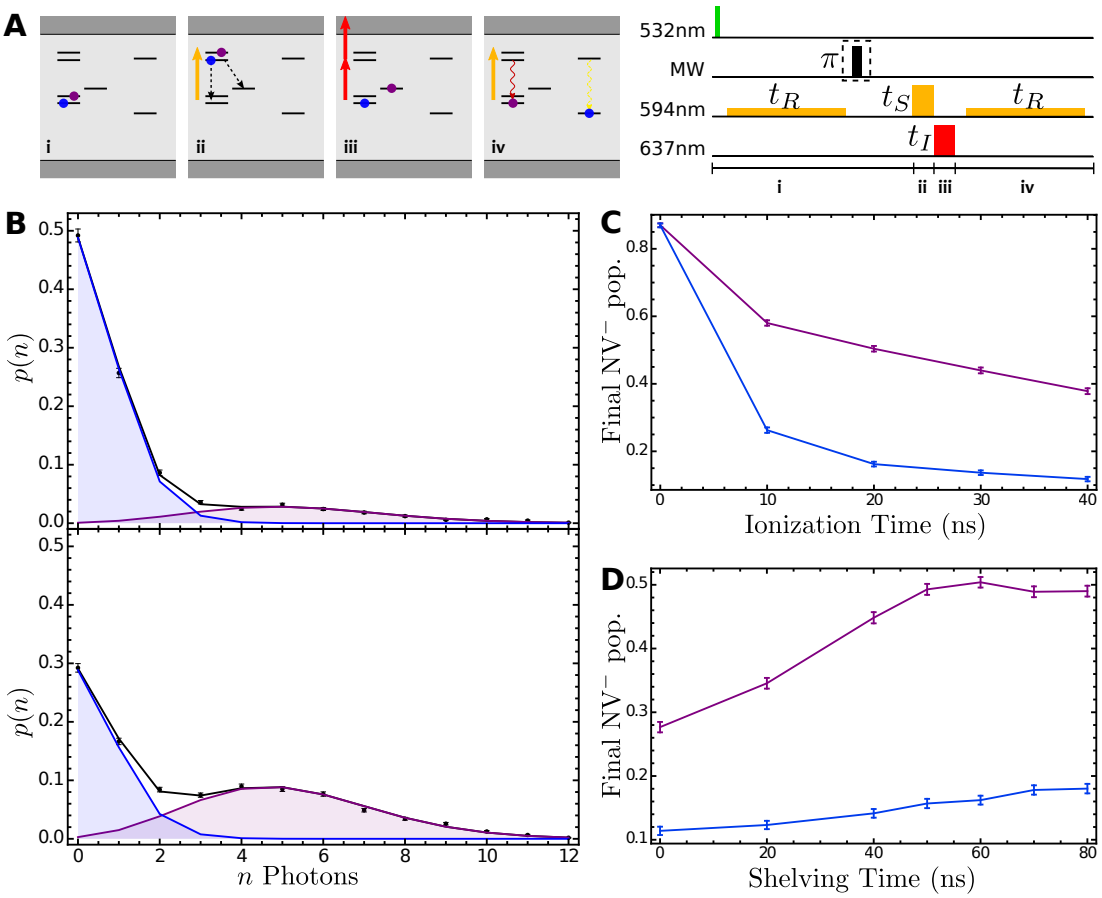

Figure 4.4: (a) Pulse sequence for spin to charge conversion measurement. The NV is prepared into $|m_s = 0\rangle$ or $|m_s = 1\rangle$ (i), after which a two step SCC sequence, consisting of (ii) a $594\,\mathrm{nm}$ shelving pulse and (iii) a $637\,\mathrm{nm}$ ionization pulse, preferentially ionizes $|m_s = 0\rangle$ to NV^0 while shelving $|m_s = 1\rangle$ into the singlet state where it is protected from ionization. Finally, a $500\,\mu\mathrm{s}$, $500\,\mathrm{nW}$ $594\,\mathrm{nm}$ pulse measures the charge state (iv). Note that for this measurement the initialization in (i) consisted of a $40\,\mathrm{ns}$, $300\,\mu\mathrm{W}$ pump pulse and a $500\,\mu\mathrm{s}$, $500\,\mathrm{nW}$ probe pulse. (b) Photon number distribution indicating the final charge state population for an initial state of $|m_s = 0\rangle$ (top, NV^- population $= 0.162 \pm 0.007$) or $|m_s = 1\rangle$ (bottom, NV^- population $= 0.504 \pm 0.009$). (c) Final NV^- population for ionization pulse durations ranging from $0\,\mathrm{ns}$ to $40\,\mathrm{ns}$ (shelving pulse fixed at $60\,\mathrm{ns}$). (c) Final NV^- population for shelving pulse durations ranging from $0\,\mathrm{ns}$ to $80\,\mathrm{ns}$ (ionization fixed at $20\,\mathrm{ns}$), showing the dynamics of the shelving process.

was also 500 µs at 500 nW.

We fit our model to the measured photon number distributions to determine the average population in NV^- at the end of the SCC step. For an initial state of $|m_s = 0\rangle$ and $|m_s = 1\rangle$, we call the average final NV^- population β_0 and β_1, respectively. The contrast between β_0 and β_1 characterizes the efficiency of the SCC mechanism. The dependence of $\beta_{0,1}$ on shelving and ionization duration is shown in Fig. 4.4c,d. In Fig. 4.4c, the shelving pulse time is fixed at 60ns and we sweep the ionization pulse time. At each ionization time point, we measure the photon number distributions for the two initial spin states to find $\beta_{0,1}$. Similarly, in Fig. 4.4d, the ionization pulse time is fixed at 20 ns and we sweep the shelving pulse time, plotting $\beta_{0,1}$ at each time point. As the shelving time is increased, the $|m_s = 1\rangle$ population is transferred to the singlet state and protected from ionization, resulting in a maximum for β_1 at 60 ns.

4.5 Spin Readout Noise

To evaluate the efficacy of the SCC mechanism as a method to read out the NV^- electron spin state, we now consider these results in the context of AC magnetometry[18]. We consider a magnetometry sequence based on a Hahn spin-echo[76], and compare the readout noise for the SCC scheme with the traditional ODMR readout mechanism. In both cases the minimum detectable magnetic field is:

$$\delta B = \frac{\pi\hbar}{2g\mu_B\sqrt{T}} \times \sigma_R \times \sqrt{\frac{\tau + t_I + t_R}{\tau^2}}, \tag{4.1}$$

where g is the electron gyromagnetic ratio, μ_B is the Bohr magneton, τ is the spin-echo time, t_I is the initialization time, t_R is the spin readout time, and T is the total measurement time for N repeated measurements each of duration $\tau + t_I + t_R$. σ_R

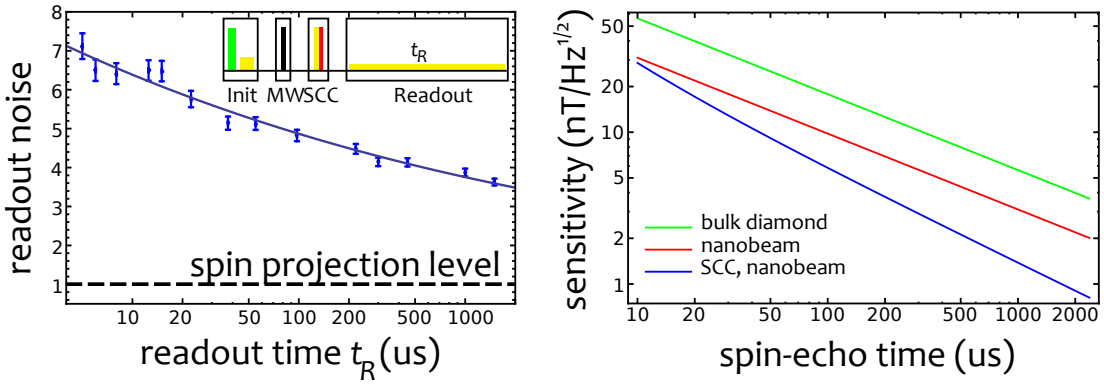

Figure 4.5: (a) The spin readout noise parameter, σ_R, is measured as a function of readout time, t_R (blue points). The pulse sequence is shown in the inset, consisting of an initialization sequence ($100\,\mathrm{ns}$ $532\,\mathrm{nm}$ pump pulse at $300\,\mu\mathrm{W}$, followed by a $900\,\mathrm{ns}$ $594\,\mathrm{nm}$ probe pulse at $11\,\mu\mathrm{W}$ to verify the charge state is NV$^-$), microwave pulse prepare in $|m_s = 0\rangle$ or $|m_s = 1\rangle$, SCC sequence ($60\,\mathrm{ns}$ $594\,\mathrm{nm}$ pulse at $135\,\mu\mathrm{W}$ followed immediately by $30\,\mathrm{ns}$ $637\,\mathrm{nm}$ pulse at $7.1\,\mathrm{mW}$), and readout for time t_R. The solid line represents a fit to the data of the form $\sigma_R(t_R) = a\sqrt{1 + b/t_R^{1/4}}$ with fit parameters a and b. (b) Projected magnetometer sensitivity as a function of spin coherence time for the SCC readout noise measured in (a) (blue curve). The projected sensitivity is found by optimizing t_R along the fitted curve for $\sigma_R(t_R)$ so as to minimize $\sigma_R(t_R)\sqrt{(\tau + t_I + t_R)/\tau^2}$, where t_I is taken to be $6.5\,\mu\mathrm{s}$ (expected initialization time $t_I = 1.5\,\mu\mathrm{s}/p_s$, where $p_s = 0.200 \pm 0.006$ is the probability of succeeding in the probe step of initialization).

is a measure of the spin readout noise for a single measurement, normalized so that $\sigma_R = 1$ for a perfect measurement (i.e. limited by only the fundamental quantum spin projection noise).

In the traditional spin readout scheme, the NV is prepared into NV^-, the Hahn spin-echo is applied for a time, τ, and the spin is read out with a short excitation pulse (typically ~ 200 ns of 532 nm light), during which time an average number of photons, $\alpha_{0,1}$, are counted when the NV is projected into $|m_s = 0, 1\rangle$, respectively. The two sources of noise in this case are spin projection noise and photon shot noise, and the overall spin readout noise is[18]:

$$\sigma_R^{trad} = \sqrt{1 + \frac{2(\alpha_0 + \alpha_1)}{(\alpha_0 - \alpha_1)^2}} \tag{4.2}$$

For a bulk diamond sample with no photonic enhancement, typical photon collection efficiencies result in a best-case value of $\sigma_R^{trad} \sim 20$[22]. With the enhanced collection efficiency from the diamond nanobeam geometry, we observe $\alpha_0 = 0.238 \pm 0.001$, $\alpha_1 = 0.154 \pm 0.002$, and $\sigma_R^{trad} = 10.6 \pm 0.3$. In both cases, photon shot noise is by far the dominant source of noise.

For the SCC spin readout mechanism, there are three sources of noise: spin projection noise, photon shot noise, and SCC noise. Because the charge readout step can be done with very high fidelity, photon shot noise is relatively less significant for the SCC scheme. Instead, the dominant source of noise is imperfect SCC efficiency. In the case of perfect charge state readout, the spin readout noise is given by:

$$\sigma_R^{SCC} = \sqrt{\frac{(\beta_0 + \beta_1)(2 - \beta_0 - \beta_1)}{(\beta_0 - \beta_1)^2}}. \tag{4.3}$$

For the $\beta_{0,1}$ values found above, the lower limit on SCC readout noise in our system is $\sigma_{R,\text{best}}^{SCC} = 2.76 \pm 0.09$. In practice, the achievable noise is somewhat higher than this due to imperfect charge state readout, which must be balanced against the time requirements for the measurement.

To evaluate the practical utility of the SCC readout, we measured $\sigma_R^{SCC}(t_R)$, using a fast initialization scheme for which the expected initialization time is 6.5 µs. In principle, there exists an optimal readout power for each t_R that minimizes $\sigma_R^{SCC}(t_R)$. To approximate this experimentally we used a set fixed set of readout powers, and first measured the ionization and photon count rates during a readout pulse under the experimental conditions (pump-probe initialization and SCC sequence). Based on these rates and the measured values of $\beta_{0,1}$, we calculated t_R that would minimize $\sigma_R^{SCC}(t_R)$ at each power, for a threshold photon number of 1, 2, 3, 4, or 6 photons. In this way, we measured a range of readout times under close to optimal conditions (see Appendix B for details).

The results are shown in Fig. 4.5a. For short $t_R \sim 5$ µs, $\sigma_R^{SCC}(t_R)$ provides a modest improvement over the traditional readout scheme, while for long readout times, $\sigma_R^{SCC}(t_R)$ approaches the SCC-limited value and provides a significant improvement. We note that the values measured for $\sigma_R^{SCC}(t_R)$ are somewhat higher than would be expected purely based on photon shot noise and our measured value of $\sigma_{R,\text{best}}^{SCC}(t_R)$. We believe this is due to the increased duty cycle employed, which may have some effect on the ionization dynamics that is not fully described by our model.

To evaluate the improvement in projected magnetometer sensitivity, we need to minimize:

$$\delta B\sqrt{T} = \frac{\pi\hbar}{2g\mu} \times \sigma_R^{SCC}(t_R) \times \sqrt{\frac{\tau + t_I + t_R}{\tau^2}} \tag{4.4}$$

with respect to t_R. To do so, we fit the measured values of $\sigma_R^{SCC}(t_R)$ with an approximate scaling function based on the photon number distribution model (Fig. 4.5a, blue curve). Using this fit and a fixed initialization time of 6.5 µs, we found the expected magnetometer sensitivity for spin coherence times ranging from 5 µs to 2 ms (at 2 ms coherence time the optimal readout time was $t_R = 575$ µs, for a projected sensitivity of 900 pT/Hz$^{1/2}$). The results are shown in Fig. 4.5b, where we have plotted the projected sensitivity for the SCC scheme in our system (blue curve), for the traditional scheme in our system (red curve), and for the traditional scheme in a bulk diamond system (green curve).

4.6 Conclusion

We have studied the ionization dynamics of the NV center on timescales commensurate with the internal spin dynamical processes of the NV^- charge state. In particular, we have demonstrated a spin-dependent ionization process that maps the spin state of NV^- onto a charge distribution between NV^- and NV^0. This mechanism provides an improvement in spin readout noise to 2.76 times the spin projection noise level, and is expected to boost single-spin magnetometer sensitivity by a factor of 4 over the previously reported sensitivity for bulk diamond[22]. In addition to applications in sensing, the SCC mechanism should provide a useful tool for NV spectroscopy, as it offers a new probe of the singlet manifold, many aspects of which remain largely unknown.

Chapter 5

Conclusion and Outlook

5.1 Interfaces between light and matter

One of the most effective means to control and observe the state of an atom is through a resonant interaction with light. Traditionally, superb control over quantum systems has required gas phase atoms trapped in vacuum chambers and isolated from any environmental effects, so that their state can be manipulated by an electromagnetic field. The same methods for manipulation are now being extended to the solid state, where atoms trapped in a crystal lattice are sufficiently well isolated from the environment to constitute stable quantum systems. Real-world applications such as nanoscale biological sensing have proven the advantages inherent to the robust and compact nature of systems such as the NV, which promises to enable a variety of practical quantum technologies. Moreover, the solid state offers tremendous potential to manipulate the atoms' electromagnetic environment by directly modifying the dielectric structure of the material. In these systems, for example, the light-matter interaction can be pushed to its natural extreme by trapping photons within the volume

of a single cubic wavelength.

5.2 NV-cavity coupling

This thesis has explored the design and fabrication of structures to observe and control solid state atoms through their interaction with light. In Chapters 2 and 3, we described the coupling of NV centers to two photonic crystal architectures, as well as tuning of an all-diamond photonic crystal cavity to the NV center ZPL. These devices have demonstrated the proof of principle for NV cavity coupling, but many challenges still remain. The modest enhancement shown is a far cry from the requirements for strong coupling, where the coherence between the NV-cavity system is preserved for a full cycle of energy transfer between the cavity photon and the atomic excitation. The NV-cavity coupling strength is exceedingly strong on account of the ultra small mode volume, however the limiting factor in this case is the cavity loss rate; the Q factor required for strong coupling is $\sim 10^5$, which is 1-2 orders of magnitude higher than has been demonstrated in existing devices. The high Q factor requirement for the NV is due in part to phonon coupling that reduces the strength of the ZPL and effectively lowers the NV-cavity coupling rate by a factor of ~ 5. This effect may be mitigated in other color centers, such as the silicon vacancy center in diamond, for which the ZPL transition is much less affected by coupling to phonon modes.

Nevertheless, true strong coupling is not an absolute requirement for many quantum applications, and the cavity parameters achieved so far are already sufficient for demonstrations of cooperative coupling[10], in which the NV is more strongly coupled to the cavity mode than to all other decay channels. In this case the key challenge is not so much to fabricate better cavities as to control the material system to maintain

good NV optical coherence in a nanofabricated device. Promising steps have been made in this direction[1], but spectral diffusion of the NV ZPL remains an outstanding hurdle that must be overcome before useful quantum technologies such as single photon sources and quantum repeaters can be realized.

5.3 Spin readout

Nanophotonic structures can also be used to channel emitted light without strongly modifying the relaxation dynamics of the emitter. In Chapter 4 we showed that diamond nanobeams can be used to boost the collected photons from an NV center and thereby improve spin readout. Additionally, unprecedented control of the NV charge state was possible. Although the internal level dynamics of the NV^- charge state, alone, provide a rich system for room temperature quantum information and sensing applications, full control of the charge state allows for improved performance, through better initialization and readout of the NV^- electron spin. Although this technique has already yielded a dramatic improvement in spin readout, further performance improvements may be possible in material systems with better charge state stability that would allow for stronger charge readout pumping and therefore faster readout. Additionally, if the technique can be made to operate uniformly across an ensemble of NVs, it could be used for ensemble sensing measurements. Further studies into the uniformity of NV ionization dynamics from center to center are needed to address these outstanding questions.

Beyond the obvious gains in spin readout noise, the rapid ionization procedure could also provide a new tool to study NV physics that is difficult to probe with conventional fluorescence measurements. For instance, extensions of the ionization pro-

cess to multi-color ionization pulses could provide a means to probe the level structure of the NV^- singlet manifold, where several excited states have been predicted but not yet observed[77]. The ability to drive from a relatively unstable energy level to a highly stable charge state may yet find unforeseen uses as a general spectroscopic tool.

5.4 Conclusion

Controlling the photonic properties of a material on the nanoscale has proven to be an invaluable tool for controlling the interaction of quantum systems with light. We have demonstrated that nanophotonic devices can dramatically alter the relaxation dynamics of a quantum emitter, and can channel its emission for efficient photon collection. These devices have already proven their utility for room temperature sensing, and hold much promise for applications in quantum computation and information and in the construction of scalable quantum networks.

Appendix A

Supporting Material for Deterministic Coupling of a Single NV Center to a Photonic Crystal Cavity

A.1 Wavelength-resolved excited state recombination rates

The excited state of the isolated NV^- decays through a set of N_j radiative channels, which we distinguish by their wavelength λ_j and describe by the recombination rate γ_j, and nonradiative recombination described by a term γ_{NR}. We consider the NV at some position $\vec{r_i}$ from the cavity, and assume that it is pumped into the excited state at some rate p_i. Then the emission spectrum at wavelength j is given by

$$I_{ij} = cp_i\eta_{ij}\frac{\gamma_{ij}}{\sum_k \gamma_{ik} + \gamma_{NR}} \tag{A.1}$$

$$= cp_i\eta_{ij}\frac{\gamma_{ij}}{\Gamma_i} \tag{A.2}$$

where η_{ij} is the collection efficiency, $\Gamma_i = \sum_k \gamma_{ik} + \gamma_{NR}$ is the excited state decay rate, and c is a proportionality constant. The term $\beta_{ij} = \gamma_{ij}/\Gamma_i$ can be identified as the fraction of the total recombination rate that occurs through wavelength j. The decay rate can be obtained from a lifetime measurement, $\Gamma_i = 1/\tau_i$. The ratio of the spectra at position i and the 'bulk position' 0 (away from the PC slab) gives:

$$\frac{I_{ij}}{I_{0j}} = \frac{p_i \eta_{ij} \gamma_{ij} \Gamma_0}{p_0 \eta_{0j} \gamma_{0j} \Gamma_i} \tag{A.3}$$

If the pump rate and collection efficiency are equal, we have

$$\frac{I_{ij}}{I_{0j}} = \frac{\gamma_{ij} \Gamma_0}{\gamma_{0j} \Gamma_i} \tag{A.4}$$

$$= F_{ij} \frac{\Gamma_0}{\Gamma_i}, \tag{A.5}$$

where the Purcell factor $F_{ij} = \gamma_{ij}/\gamma_{0j} = I_{ij}\Gamma_i / I_{0j}\Gamma_0$. For a position $i = 1$ where the NV and cavity are aligned on top of each other, $F_{1j} = F(\lambda_j)$ is plotted in Figure A.2.

A.2 Photon correlation measurements

The photon correlation measurement is performed with a Hanbury Brown / Twiss (HBT) setup. The PL is directed to a beam splitter, after which the two arms are coupled through single mode fibers (SMF) to single photon detector modules (Perkin Elmer). A time-correlated counting module is used to assemble the histogram of clicks on the two detectors. Figure A.1 shows the spectra collected through the SMF for the coupled and uncoupled positions of the cavity.

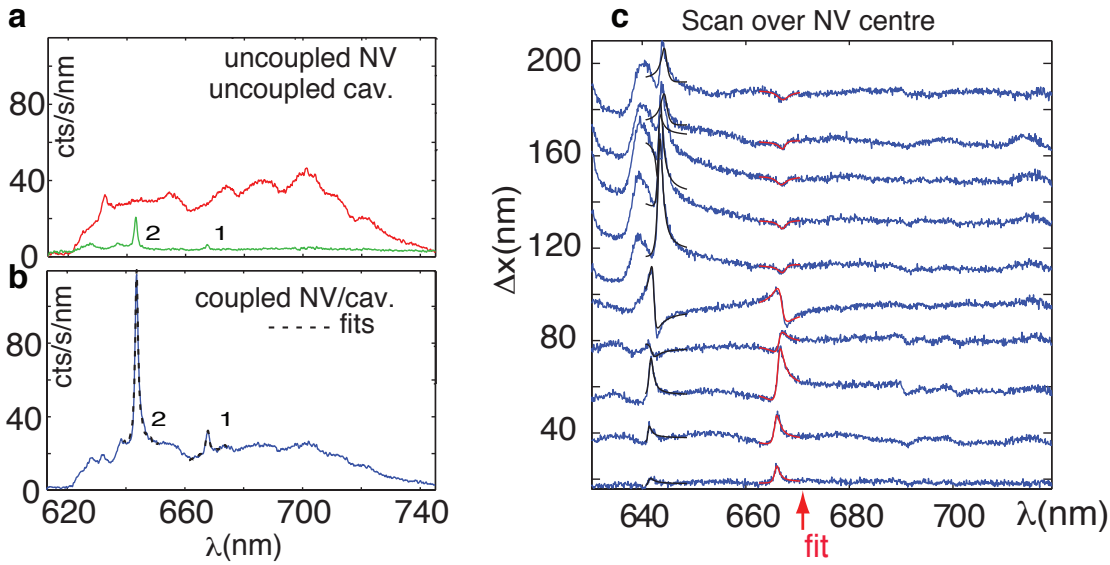

Figure A.1: Spectra collected into single mode fiber. (a) PL from uncoupled NV and cavity. (b) PL from cavity-coupled NV centre. (c) Scanning the cavity over the NV centre produces interference effects between NV and cavity emission. Fits to Equation 2.1 with $C_{int} = 0.6$.

A.3 Characterization of cavity modes

To further characterize the cavity resonances experimentally, we measured the polarization dependence of the emission collected from two different locations while pumping the NV near the center of the cavity. These positions are indicated as x_1 and x_2 in Figure A.3(a), together with the simulated electric field energy density for three relevant cavity modes. Collecting from the pump location x_2, we observe the mode at 667 nm to be strongly polarized, while the mode at 643 nm exhibits only weak polarization dependence (Figure A.3(b)), for a total of three modes. From x_1, we only observe polarized modes at λ_1 and λ_2. From these observations, we conclude that the peak at λ_2 corresponds to the two modes shown in Figure A.3(a.1,a.2) with nearly degenerate frequency (within the relatively broad linewidth), opposite polarization, and

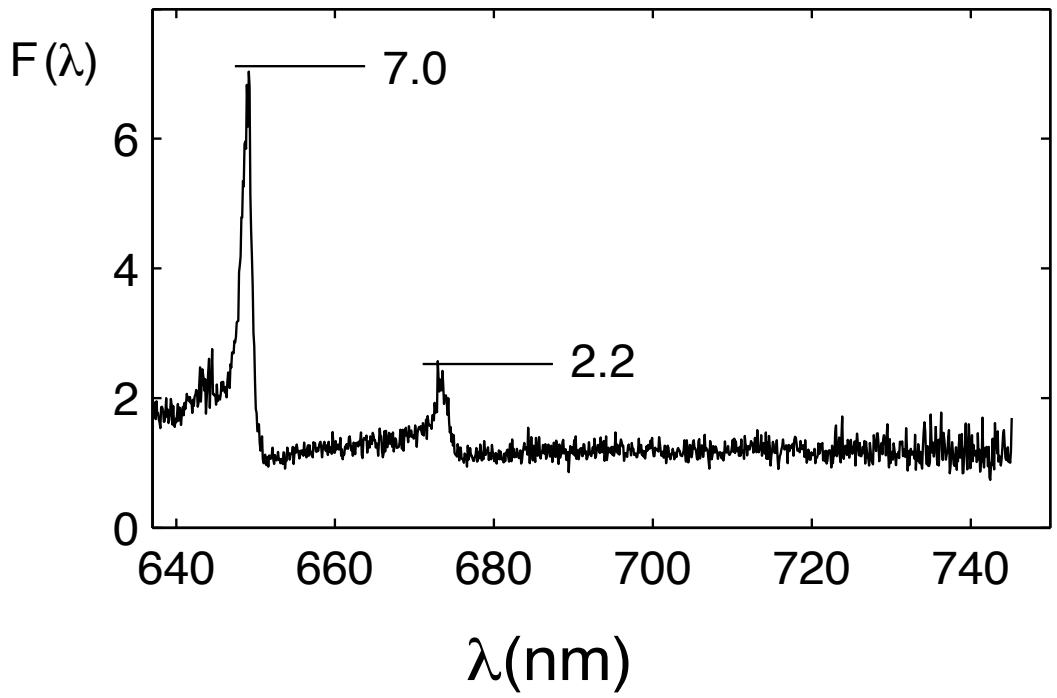

Figure A.2: The calculated spontaneous emission rate modification $F(\lambda)$.

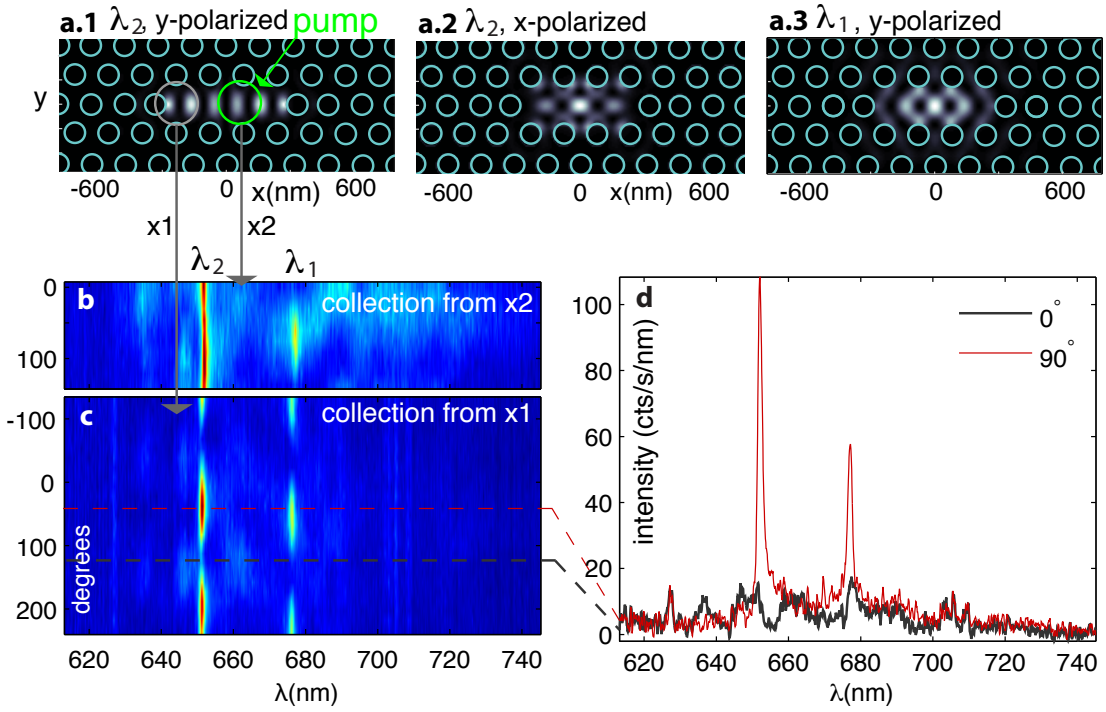

Figure A.3: Polarization dependence of cavity emission collected from spatially distinct points. We position the cavity so that it slightly off-center from the NV emitter. Exciting the NV and collecting from the point of excitation (a) we observe the fluorescence at $667\,\mathrm{nm}$ to be strongly polarized while the fluorescence at $643\,\mathrm{nm}$ is only slightly polarized. However, by collecting from the end of the cavity in (b-c), we can pick out the resonance at $643\,\mathrm{nm}$ which is polarized along the same axis as the $667\,\mathrm{nm}$ mode.

different spatial extent. The peak at λ_1 indeed corresponds to a single mode, which we identify as the lowest-frequency confined state of the L3 cavity.

A.4 Single mode fiber spectra

When the multi-mode fiber was replaced with a single mode fiber, the spectra in Figure 2(c,d) in the main text show the same pattern, but at a reduced count rate, as displayed in Figure A.1.

The simultaneous collection from the cavity and the emitter results in interference at the detector. As the cavity is scanned over the NV emitter, we observe Fano-like features at the cavity resonances shown in Figure A.1(b), which are fit well by Equation 2.1 with $C_{int} = 0.6$. Such interface effects have been described before in microdisks[44] and microspheres[78] coupled to single NV emitters. In microscopy, the intereference signature may be used to better distinguish a single emitter from the background.

A.5 Filtered cavity emission photon statistics

To verify that the cavity emission corresponding to peak 2 originates from a single NV center, this emission was filtered with a grating setup to 1 nm. The filtering introduces considerable loss and reduced the signal so that a reliable autocorrelation measurement was not possible. Instead, we performed a cross-correlation between the filtered cavity emission and the total emission between 630-700 nm. This measurements is shown in Figure A.4 and clearly indicates that both filtered and unfiltered light originate from a single NV center.

A.6 Electron Spin Resonance and Rabi Oscillations

The NV center has two unpaired electrons in a triplet configuration with a zero-field splitting of $\Delta = 2.87\,\text{GHz}$ between $m_s = 0$ and $m_s = \pm 1$ sublevels. The excited state decay rates allow spin-sensitive detection since the fluorescence is reduced for the $m_s = \pm 1$ states[79]. In the spin measurements described here, the $m_s = \pm 1$ sublevels were additionally split by an external magnetic field produced by a permanent magnet. Figure A.5(a) shows the microwave transitions from $m_s = 0$ to $m_s = \pm 1$,

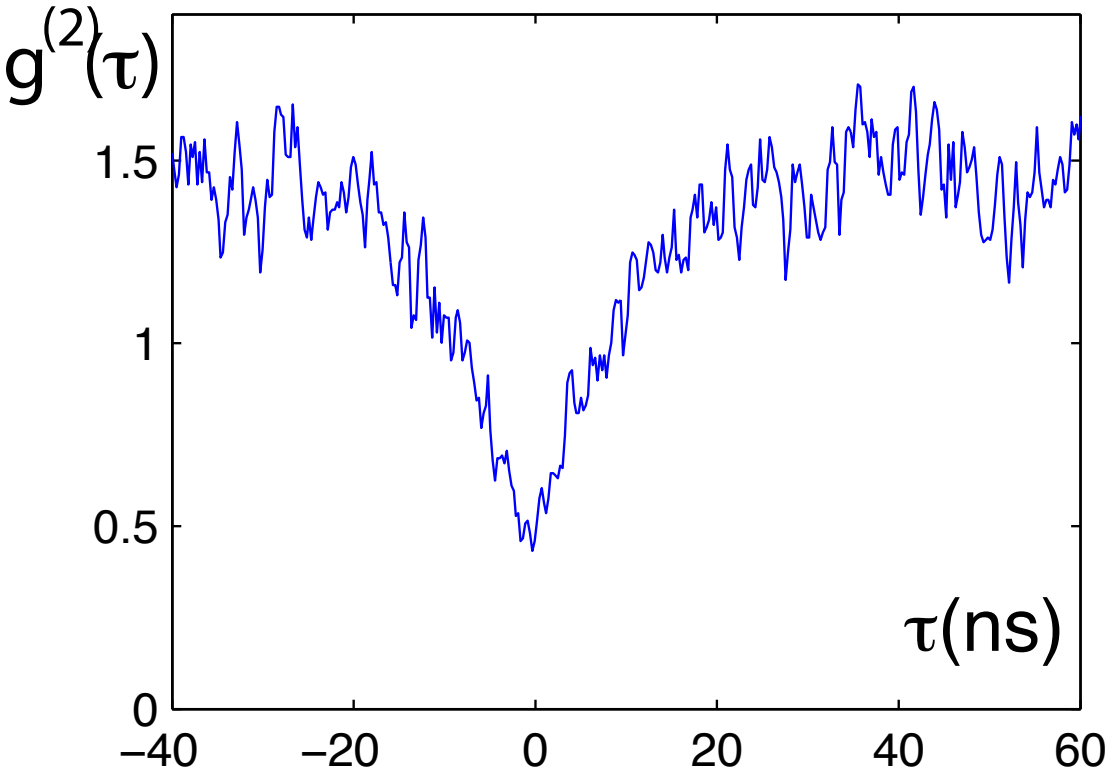

Figure A.4: Cross-correlation between the filtered cavity emission and the total emission.

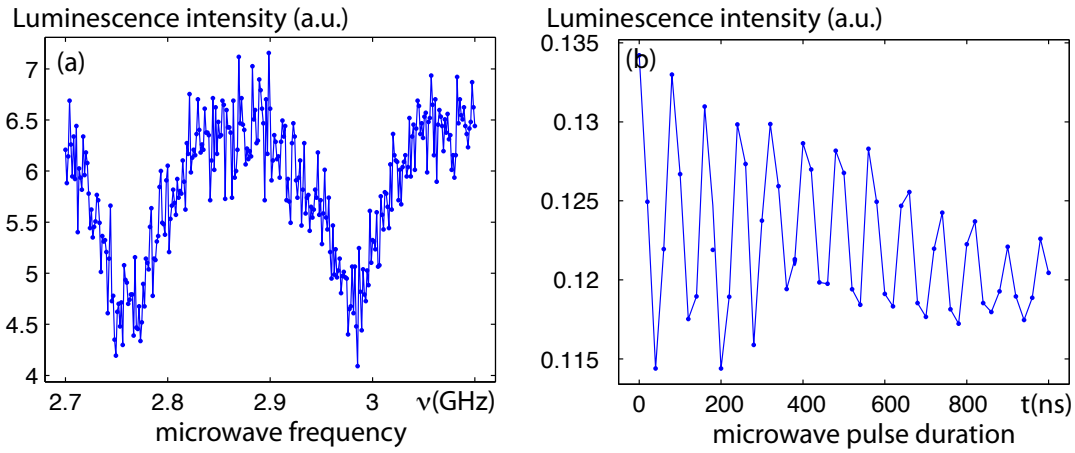

Figure A.5: (a) Spin transition observed in the NV fluorescence under excitation with a microwave field at frequency ν. (b) Driven spin oscillations for $\nu = 2.77\,\mathrm{GHz}$.

which are evident in the intensity of the cavity-coupled NV as a function of a microwave field of intensity ν, while Figure A.5(b) shows driven spin oscillations when the NV spin is optically initialized in $m_s = 0$, excited with a microwave pulse for a duration t at a frequency $\nu = 2.77\,\mathrm{GHz}$, and optically detected using a pulse sequence described in elsewhere[80].

A.7 Spontaneous emission modification

The Hamiltonian describing a NV (lowering operator $\sigma = |g\rangle\langle e|$) coupled to a cavity mode (with annihilation operator a, without considering environment interactions, is given by

$$H = \frac{\Delta}{2}a^\dagger a - \frac{\Delta}{2}(\sigma_z) + ig(\sigma a^\dagger - a\sigma^\dagger), \tag{A.6}$$

where Δ is NV-cavity detuning and the reference energy is the mean of NV and cavity energy.

The Master equation is given by

$$\frac{d\rho}{dt} = -i[H,\rho] + \frac{\kappa}{2}(2a\rho a^\dagger - a^\dagger a\rho - \rho a^\dagger a) + \frac{\gamma}{2}(2\sigma\rho\sigma^\dagger - \sigma^\dagger\sigma\rho - \rho\sigma^\dagger\sigma) + \frac{\gamma_d}{2}(\sigma_z\rho\sigma_z - \rho) \quad \text{(A.7)}$$

where γ, κ and γ_d account for NV population decay, cavity population decay and NV pure dephasing; and $\sigma_z = [\sigma^\dagger, \sigma]$.

We consider the subspace of 0 or 1 excitation in the NV $|g\rangle, |e\rangle$, and 0 or 1 excitations in the cavity $|0\rangle, |1\rangle$. From Equation A.7 we obtain the Maxwell Bloch equations[81]

$$\left\langle \frac{da}{dt} \right\rangle = (-i\frac{\Delta}{2} - \frac{\kappa}{2})\langle a\rangle + g\langle\sigma\rangle \quad \text{(A.8)}$$

$$\left\langle \frac{d\sigma}{dt} \right\rangle = (i\frac{\Delta}{2} - \frac{\gamma}{2} - \gamma_d)\langle\sigma\rangle + g\langle\sigma_z a\rangle \quad \text{(A.9)}$$

$$\quad \text{(A.10)}$$

These two coupled equations are solved with the initial condition $a(0) = 0, \sigma(0) = 1$; $\langle\sigma_z a\rangle = -a$ in the subspace considered here. We define $c_1 = \left(-i\frac{\Delta}{2} - \frac{\kappa}{2}\right)$ and $c_2 = \left(i\frac{\Delta}{2} - \frac{\gamma}{2} - \gamma_d\right)$ and $\lambda_- = c_1 + c_2 - \sqrt{(c_1 - c_2)^2 - 4g^2}$, $\lambda_+ = c_1 + c_2 + \sqrt{(c_1 - c_2)^2 - 4g^2}$. The time-dependent solution is

$$a(t) = \frac{(e^{\lambda_+ t} - e^{\lambda_- t})g}{\sqrt{(c_1 - c_2)^2 - 4g^2}} \quad \text{(A.11)}$$

and

$$\sigma(t) = \frac{(c_1 - c_2)(e^{\lambda_- t} - e^{\lambda_+ t}) + \sqrt{(c_1 - c_2)^2 - 4g^2}(e^{\lambda_- t} + e^{\lambda_+ t})}{2\sqrt{(c_1 - c_2)^2 - 4g^2}} \quad \text{(A.12)}$$

The electric field emitted by the NV and cavity is described by

$$E^{(+)} = \sqrt{\gamma}\sigma\hat{e}_{NV} + \sqrt{\kappa}a\hat{e}_c + c.c., \tag{A.13}$$

where $\hat{e}_{NV}$ and $\hat{e}_c$ describe the spatial profiles of the emission from the NV center and the cavity. The emission is collected through a lens into an optical fiber (either single mode or multi-mode) with a set of orthonormal modes $\{\hat{f}(\vec{k},\omega)\}$. The field at the output of the fiber, which is directed at the detector, is given by

$$E'^{+} = U_F(\sqrt{\gamma}\sigma\hat{e}_{NV} + \sqrt{\kappa}a\hat{e}_c), \tag{A.14}$$

where $U_F = \sum_{\vec{k},\omega}(\cdot\hat{f}(\vec{k},\omega))(\hat{f}(\vec{k},\omega)\cdot)$. The spectrum is obtained from the Quantum Regression theorem, $S(\omega) \propto \int_{-\infty}^{\infty}\int_{0}^{\infty}\langle E'^{+}(t)E'^{-}(t')\rangle\, dtdt'$. We make the assumption that the linewidth of the NV center is much broader than the NV-cavity detuning and all other loss or coupling rates: $\omega = \omega_c, \kappa \ll \gamma_d, g \ll \gamma_d, \kappa$. After normalizing the spectrum by the bare NV emission spectrum, we obtain

$$\begin{aligned} S'(\omega) \quad \propto \quad & \hat{e}_{NV}U_F\hat{e}_{NV} + 2\Re[\hat{e}_{NV}U_F\hat{e}_c e^{i\Delta\phi}\sqrt{f^c(\vec{r})}\frac{1}{1+i(\omega-\omega_c)/\kappa}] + \\ & \hat{e}_c U_F\hat{e}_c f^c(\vec{r})|\frac{1}{1+i(\omega-\omega_c)/\kappa}|^2, \end{aligned} \tag{A.15}$$

where $F = (g(\vec{r},\vec{\mu}))^2/\kappa\gamma$ denotes the Purcell factor at position $\vec{r}$ and orientation $\vec{\mu}/|\vec{\mu}|$ of the NV in the field of the cavity. In this experiment, it is not possible to calculate the term $\hat{e}_{NV}U_F\hat{e}_c$ directly because of uncertainty in the coupling of the NV and cavity modes to the fiber. In general, we therefore represent the detected spectrum as

$$S_d(\omega) = C_1 + 2C_2\Re[e^{i\Delta\phi}\sqrt{f^c(\vec{r})}\frac{1}{1+i(\omega-\omega_c)/\kappa}] + C_3 f^c(\vec{r})|\frac{1}{1+i(\omega-\omega_c)/\kappa}|^2,$$

where the real coefficients C_i are obtained by fits to the data. We obtain good fits for the single mode fiber with $C_2/C_1 \sim 0.6$, and for the multi-mode fiber with $C_2/C_1 \sim 0$.

A.8 Imaging of general samples

The signal $PL(\omega, \vec{r})$ in Fig. 3 in the main text represents the convolution of the emitter's spatial profile, $e(\vec{r})$, and the spectrometer signal given in Equation 2.1. Thus, $PL(\omega, \vec{r}) = \int e(\vec{r} - \vec{r}')S_d(\omega, \vec{r}')dl'$, where dl' is the displacement along the path of $\vec{r}'$. Since the NV center is less than 1 nm in size, we consider it as a delta function, so thfat $PL(\omega, \vec{r}) = S_d(\omega, \vec{r})$, giving the response function of our scanning probe. Once this response function is known, the SCN maps a general sample $e'(\vec{r})$ by first measuring the convolved image $PL'(\vec{r})$ and then deconvolving by the known response $S_d(\omega, \vec{r}')$ to obtain $e'(\vec{r})$.

Appendix B

Supporting Material for Spin to Charge Conversion in NV Centers

B.1 Device Fabrication and Photonic Properties

To overcome the collection efficiency limitations in bulk diamond samples, we employed an angled RIE fabrication technique[64] to carve 300 nm-wide, triangular cross-section nanobeams from a bulk diamond sample. To do so, we began with a polished diamond sample (Element6, type IIa, 1ppm N concentration) and removed $\sim$ 600 nm of material from the top surface in a top-down oxygen RIE step. Next, we spun a PMMA layer onto the diamond and patterned the beam mask shape via e-beam lithography. After developing the PMMA, a 294 nm-thick layer of Al_2O3 was sputtered and the PMMA was stripped, transferring the etch mask pattern into the Al_2O3 layer. We then did a top-down etch for 3 min with O_2, followed by a 3 min etch with O_2 + Cl_2, broken into 12 cycles of 15 s each. The diamond was then cleaned in a boiling solution of 1:1:1 perchloric, nitric, and sulfuric acids, and annealed in a 3-stage

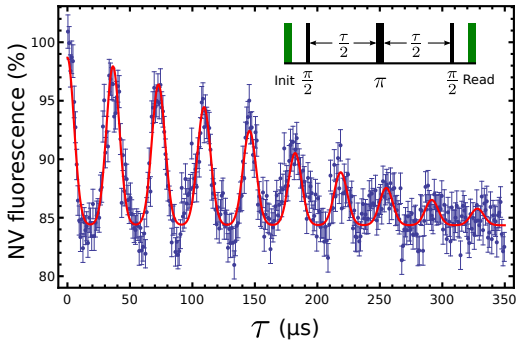

Figure B.1: Spin echo for NV in nanobeam. The blue points are fluorescence measured after a Hahn spin-echo, normalized to the fluorescence level with no spin-echo pulses. The red curve is a fit to the data (see text).

ramp consisting of 3 h ramp from room temperature to 400 °C, annealing at 400 °C for 4 h, 3 h ramp from 400 °C to 800 °C, annealing at 800 °C for 8 h, 12 h ramp from 800 °C to 1200 °C, anneal at 1200 °C for 2 h, ramp down to room temperature. Following the anneal the diamond was again acid cleaned and baked at 465 °C in oxygen environment.

To maximize collection efficiency, we transferred the beams to a glass coverslip for imaging with an oil immersion objective (Nikon, 1.49 NA). Using finite-difference-time-domain simulations, we found that the collection efficiency from such a structure can vary strongly with beam diameter and NV placement within the beam, but is expected to be as high as 60% for NVs near the diamond-glass interface. We expect the collection efficiency to be higher in thinner beams, but experimentally we found the NVs to be unstable, and so we used ~ 300 nm beams for the experiment.

B.2 NV Spin Coherence

For NV centers in the nanobeams, we observed similar spin coherence properties to NV centers in bulk, natural ^{13}C abundance diamond[80]. A Hahn spin-echo measure-

ment is shown in Fig. B.1 for an NV in a similarly prepared beam as that which was used for the SCC measurements. The data was fitted by the function[80]:

$$F(\tau) = A + Be^{-(\tau/T_2)^n} \sum_{j=0}^{9} e^{-((\tau - jT_{rev})/T_{dec})^2}, \tag{B.1}$$

with $A = 0.844 \pm 0.001$, $B = 0.143 \pm 0.005$, $n = 1.72 \pm 0.14$, $T_{rev} = 36.48 \pm 0.04\mu$s, $T_{dec} = 7.47 \pm 0.22\mu$s, and $T_2 = 201 \pm 7\mu$s.

B.3 Model for photon statistics

For the charge state measurements described in Chapter 4, we assumed that the dynamics can be fully described by 4 rates: the ionization rates from NV^- to NV^0 and vice versa (g_1 and g_0, respectively), and the photon count rates when in NV^- and NV^0 (γ_1 and γ_0, respectively). From $\gamma_{1,0}$, we can calculate the photon number distribution that results from a particular sequence of ionization events. For example, if the NV begins in NV^-, jumps to NV^0 after time τ_1, then jumps back to NV^- after an additional time t_1 and remains in NV^- for the rest of the counting window, the resulting photon number distribution for that ionization sequence would be a Poisson distribution with average photon number $\gamma_1(t_R - t_1) + \gamma_0 t_1$. The total photon number distribution for a particular initial charge state and total counting time t_R is then a sum over all possible ionization sequences, weighted by the probability for each sequence to occur. In the case that the initial state is NV^-, we have:

$$\begin{aligned} p(n|\mathrm{NV}^-, \mathrm{odd}) \;=\; & \int_0^{t_R} d\tau e^{(g_0-g_1)\tau - g_0 t_R} \sum_{i=1}^{\infty} g_1^i g_0^{i-1} \prod_{j=1}^{i-1} \int_0^{\tau - \sum_{k=1}^{(j-1)} \tau_k} ds_j \times \\ & \prod_{j=1}^{i-1} \int_0^{(t_R-\tau) - \sum_{k=1}^{(j-1)} t_k} dt_j \mathrm{PoissPDF}(\gamma_1\tau + \gamma_0(t_R - \tau), n) \end{aligned} \tag{B.2}$$

$$
\begin{aligned}
p(n|\mathrm{NV}^-,\mathrm{even}) &= \int_0^{t_R} d\tau e^{(g_0-g_1)\tau-g_0 t_R}\sum_{i=1}^{\infty}(g_1 g_0)^i \prod_{j=1}^{i}\int_0^{\tau-\sum_{k=1}^{(j-1)}\tau_k} d\tau_j \times \\
&\quad \prod_{j=1}^{i-1}\int_0^{(t_R-\tau)-\sum_{k=1}^{(j-1)}t_k} dt_j \mathrm{PoissPDF}(\gamma_1\tau+\gamma_0(t_R-\tau),n) \\
&\quad + e^{-g_1 t_R}\mathrm{PoissPDF}(\gamma_1 t_R, n) \qquad \text{(B.3)}
\end{aligned}
$$

where τ is the total time spent in NV^- and must therefore be integrated over $[0, t_R]$, $\mathrm{PoissPDF}(x, n)$ is the probability distribution function for an outcome of n for a Poisson random variable with mean value x, and we have broken the result into those cases where there are an even total number of ionization events and and odd number. The last term in the expression for $p(n|\mathrm{NV}^-, \mathrm{even})$ is the zero ionization event case. For the case of NV^0 as the initial state, simply exchange $1 \leftrightarrow 0$. The integral products can be evaluated as the volume of a pyramid in i dimensions, and consequently the sum over ionization events reduces to a relatively simple expression in terms of Bessel functions:

$$
\begin{aligned}
p(n|\mathrm{NV}^-,\mathrm{odd}) &= \int_0^{t_R} d\tau g_1 e^{(g_0-g_1)\tau-g_0 t_R}\mathrm{BesselI}(0, 2\sqrt{g_1 g_0 \tau(t_R-\tau)}) \qquad \text{(B.4)} \\
p(n|\mathrm{NV}^-,\mathrm{even}) &= \int_0^{t_R} d\tau \sqrt{\frac{g_1 g_0 \tau}{t_R-\tau}} e^{(g_0-g_1)\tau-g_0 t_R}\mathrm{BesselI}(1, 2\sqrt{g_1 g_0 \tau(t_R-\tau)}) \\
&\quad + e^{-g_1 t_R}\mathrm{PoissPDF}(\gamma_1 t_R, n), \qquad \text{(B.5)}
\end{aligned}
$$

where $\mathrm{BesselI}(n, x)$ is a modified Bessel function of the first kind. To evaluate these photon number distributions, we performed the integral numerically in *Mathematica*.

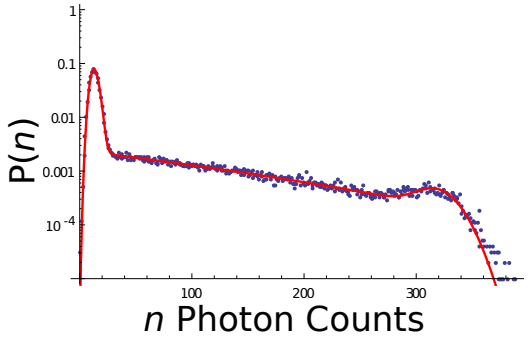

Figure B.2: Example of model for photon statistics. Data was taken under 875 nW illumination with cw 594 nm light, integration time 8 ms. 100,000 measurements.

B.4 Measuring ionization and photon count rates

The above model can be used to find the ideal power and time settings to maximize $\mathcal{F}_C$, but first we need to find the ionization and photon count rates. To do so, we integrated the counts over a time window $T \sim 1/g_1(P)$ for a range of cw 594 nm powers, P, and used the model to fit the photon number distribution from 100,000 measurements. The choice of T is made to ensure that sufficient ionization events occur to get an accurate fit of the ionization rates. Since the measurement was steady state, it is sufficient to select T to be long enough to measure g_1, since $g_{0,1}$ are related by the steady state population balance: $g_0/g_1 = p(NV^-)/p(NV^0)$. An example of the model fitted to data taken at 875 nW for 8 ms integration times is shown in Fig. B.2.

The rates measured via the above fitting procedure for cw 594 nm powers from 875 nm to 14.5 µW are shown in Fig. B.3 (blue points). The count rates are fitted by an expression of the form $a * P/(1 + P/P_{sat}) + dc$ where P_{sat} is the saturation power and dc is the detector dark count rate, measured to be 0.268 kcps. The ionization rates are fitted by an expression of the form $aP^2/(1 + P/P_{sat})$, where P_{sat} is taken from the corresponding photon count rate fit.

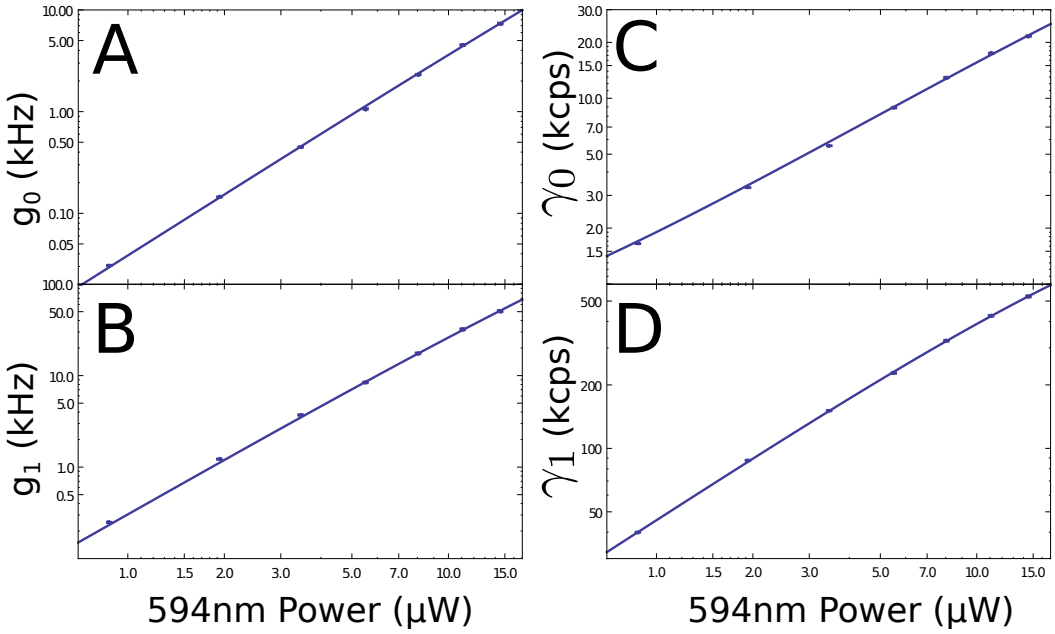

Figure B.3: Ionization and photon count rates under cw $594\,\mathrm{nm}$ illumination. (a) g_0, fitted with a model of the form $aP^2/(1+P/P_{sat})$ with $P_{sat} = 134\,\mu\mathrm{W}$, $a = 39$ cps/μW^2. (b) g_1, fitted with a model of the form $aP^2/(1+P/P_{sat})$ with $P_{sat} = 53.2\,\mu\mathrm{W}$, $a = 310$ cps/μW^2. (c) γ_0, fitted with a model of the form $a*P/(1+P/P_{sat})+dc$, with detector dark count rate $dc = 0.268$ kcps measured independently, $a = 1.65$ kcps/μW, $P_{sat} = 134\,\mu\mathrm{W}$. (d) γ_1, fitted with a model of the form $a*P/(1+P/P_{sat})+dc$, with $a = 46.2$ kcps/μW, $P_{sat} = 53\,\mu\mathrm{W}$. 100,000 measurements were taken at all power levels. Saturation power levels were determined from fits to the $\gamma_{0,1}$ data and the fitted values were then used for the fits of $g_{0,1}$.

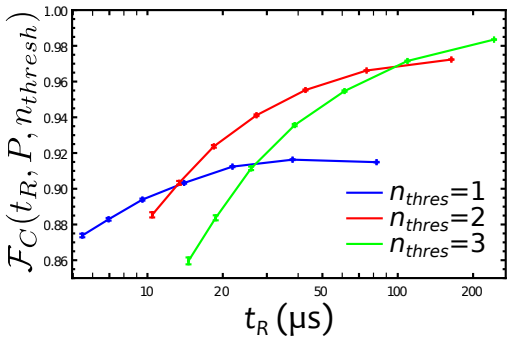

Figure B.4: Calculated optimal $\mathcal{F}_C$ for a range of powers at photon thresholds $n_{thresh} = [1, 2, 3]$. For each power and threshold combination, the readout time is optimized to maximize $\mathcal{F}_C$.

B.5 Optimal readout time

With the power-dependent rates measured (Fig. B.3), we can now determine the optimal readout times and corresponding $\mathcal{F}_C(P, t_R)$. To do so, we use a simple thresholding algorithm ($n \geq n_{thresh} \rightarrow NV^-$, $n < n_{thresh} \rightarrow NV^0$) under the assumption of a 50/50 charge state population balance. Then, using the photon distribution from the above model, we calculate the probability of correctly determining the charge state, and maximize that outcome with respect to t_R for each power, using a photon threshold of $n_{thresh} = [1, 2, 3]$. The resulting 3 data sets (one for each photon threshold) are shown in Fig. B.4

B.6 Magnetometer sensitivity

We consider the following scheme for sensing AC magnetic fields with an NV:

1. initialize the NV into $|m_s = 0\rangle$, in time t_I,
2. carry out a spin-echo pulse sequence occupying time τ,
3. read out the NV spin, in time t_R.

4. The experiment may be repeated a number of times, N, so that the aggregate measuring time is $T = N(\tau + t_I + t_R)$.

At the end of the spin-echo sequence, the state of the system is

$$|\psi(\tau)\rangle = \cos\left(\frac{g\mu_B B\tau}{\pi\hbar}\right)|\mathrm{m_s}=0\rangle - i\sin\left(\frac{g\mu_B B\tau}{\pi\hbar}\right)|\mathrm{m_s}=1\rangle, \tag{B.6}$$

where g is the electron Landé g factor and B is the magnitude of the magnetic field. The measurement procedure projects onto one or another of $|\mathrm{m_s}=0\rangle, |\mathrm{m_s}=1\rangle$, with probabilities:

$$p_0 = \cos^2\left(\frac{g\mu_B B\tau}{\pi\hbar}\right) \tag{B.7}$$

$$p_1 = 1 - p_0 = \sin^2\left(\frac{g\mu_B B\tau}{\pi\hbar}\right). \tag{B.8}$$

During the measurement we count the number of photons collected from the NV. For each shot, the photon number distribution depends on the projected spin state. Let us denote the photon number distributions for the two states $D_0(n)$ and $D_1(n)$, where the index refers to the projected spin state. Thus, the expected distribution for a measurement of the superposition state $|\psi(\tau)\rangle$ (eq. B.6) will be:

$$P(n) = p_0 D_0(n) + p_1 D_1(n). \tag{B.9}$$

The minimum detectable change in the magnitude of the magnetic field, δB, is that which shifts the average photon number, $S = \langle n\rangle$, by the width, σ_S, of the photon number distribution:

$$\delta B = \frac{\sigma_S}{\partial S/\partial B} = \frac{\pi\hbar}{g\mu_B\tau}\frac{\sigma_S}{\langle D_0\rangle - \langle D_1\rangle}, \tag{B.10}$$

where we have taken $p_0 = p_1 = 1/2$ to maximize the slope of the signal with respect to a change in magnetic field amplitude. Thus far we have considered a single measurement, but we may average over N measurements to obtain $1/\sqrt{N}$ improvement in the sensitivity. In general, then*:

$$\delta B = \frac{\pi\hbar}{2g\mu_B\sqrt{T}} \times \sigma_R \times \sqrt{\frac{\tau + t_I + t_R}{\tau^2}}. \tag{B.11}$$

where we have defined $\sigma_R = \frac{2g\mu_B\tau}{\pi\hbar}\frac{\sigma_S}{\partial S/\partial B}$ to be the single-shot readout noise, normalized so that for a measurement where spin projection noise is the only source of uncertainty, $\sigma_R = 1$. In general, σ_R will be a function of t_I and t_R, so that improvements in σ_R must be balanced with the associated requirements in overhead time.

B.6.1 Readout Noise

We now derive an expression for σ_R in the case of spin readout based on the SCC mechanism. The procedure consists of two steps: first the the spin state is converted to a charge state and second the charge state is read out.

The SCC efficiency is characterized by two parameters for the likelihood to be converted to NV^- from an initial state of either $|m_s = 0\rangle$ or $|m_s = 1\rangle$. We will call β_0 the probability that an initial spin state of $|m_s = 0\rangle$ is converted to a charge state of NV^-, and β_1 the probability that an initial spin state of $|m_s = 1\rangle$ is converted to NV^-.

The charge state detection consists of counting photons, and results in a photon number distribution $D^0(n)$ or $D^-(n)$, depending on whether the NV begins the readout timewindow in NV^0 or NV^-, respectively. These distributions can be approxi-

*I find it helpful to keep in mind that $\frac{\pi\hbar}{2g\mu_B} = 8.9\,\mathrm{pT\,Hz^{-1}}$.

mately Poissonian for short measurements times, but in general they will be a mixture of Poissonian distributions, as described by the photon statistics model, since the NV can undergo ionization or recombination over the course of the measurement. Nevertheless, we can consider the mean photon number, $\langle D^- \rangle$, $\langle D^0 \rangle$, and variance, $\sigma^2_{D^-}$, $\sigma^2_{D^0}$, for the two distributions.

We can now write the overall photon number distribution for the measurement signal, taking into account all possible combinations of spin projection, SCC, and charge state readout:

$$P(n) = p_0(\beta_0 D^-(n) + (1-\beta_0)D^0(n)) + (1-p_0)(\beta_1 D^-(n) + (1-\beta_1)D^0(n)) \quad \text{(B.12)}$$

We now compute σ_R for measurement conditions where $p_0 = p_1 = 1/2$:

$$\begin{aligned}
\sigma_R^{SCC} &= \frac{2g\mu_B\tau}{\pi\hbar}\frac{\sigma_S}{\partial S/\partial B} && \text{(B.13)}\\
S &= p_0(\beta_0\langle D^-\rangle + (1-\beta_0)\langle D^0\rangle) + (1-p_0)(\beta_1\langle D^-\rangle + (1-\beta_1)\langle D^0\rangle)\\
&= \frac{\beta_0+\beta_1}{2}\langle D^-\rangle + \left(1 - \frac{\beta_0+\beta_1}{2}\right)\langle D^0\rangle && \text{(B.14)}\\
\frac{\partial S}{\partial B} &= \frac{g\mu_B\tau}{\pi\hbar}(\beta_0-\beta_1)(\langle D^-\rangle - \langle D^0\rangle) && \text{(B.15)}\\
\sigma_S^2 &= \left[\sum_{n=0}^{\infty} n^2 P(n)\right] - S^2\\
&= \frac{1}{4}(\beta_0+\beta_1)(2-\beta_0-\beta_1)(\langle D^-\rangle - \langle D^0\rangle)^2\\
&\quad + \frac{\beta_0+\beta_1}{2}\sigma^2_{D^-} + \left(1-\frac{\beta_0+\beta_1}{2}\right)\sigma^2_{D^0} && \text{(B.16)}\\
\sigma_R^{SCC} &= \sqrt{\frac{(\beta_0+\beta_1)(2-\beta_0-\beta_1)}{(\beta_0-\beta_1)^2}} \times\\
&\quad \sqrt{1 + 2\frac{\sigma^2_{D^-}/(2-\beta_0-\beta_1) + \sigma^2_{D^0}/(\beta_0+\beta_1)}{(\langle D^-\rangle - \langle D^0\rangle)^2}} && \text{(B.17)}
\end{aligned}$$

This final expression for σ_R is completely general. It contains the fundamental quantum spin projection noise, as well as the noise associated with the SCC step and the charge state readout. In the limit that $D^-(n)$ and $D^0(n)$ are well separated, the readout noise is dominated by the SCC efficiency:

$$\sigma_R^{SCC} \approx \sqrt{\frac{(\beta_0+\beta_1)(2-\beta_0-\beta_1)}{(\beta_0-\beta_1)^2}}. \tag{B.18}$$

This expression represents the best possible spin readout noise for a given SCC efficiency. We can measure β_0 and β_1 (thereby experimentally determining the limit in eq. B.18) by building up enough statistics to reconstruct the photon number distribution when the NV is prepared in $|m_s = 0\rangle$ or $|m_s = 1\rangle$. In practice, however, the contributions of imperfect charge state readout prevent us from measuring at the limit in eq. B.18. Instead, the relevant value of σ_R is determined by measuring effective SCC efficiencies, $\tilde{\beta}_{0,1}$, defined as the probability of measuring an outcome of NV^- for an initial state of $|m_s = 0\rangle$ or $|m_s = 1\rangle$, respectively. For that measurement, we set a threshold photon number, and a result above or equal to threshold corresponds to an outcome of NV^-. We repeated the measurement 100,000 times, post-selected for the measurement of a probe photon, and estimated $\tilde{\beta}_{0,1}$ as the fraction of NV^- outcomes. We used these values to determine the measured values of $\sigma_R^{SCC}(t_R)$ in Fig. 4.5.

B.7 Measuring readout noise vs. readout time

To measure the dependence of σ_R^{SCC} with t_R, we again used the measured ionization and photon count rates and and the photon statistics model to find the optimal t_R that minimizes σ_R^{SCC}, for a set of readout laser powers, at photon thresholds of 1,

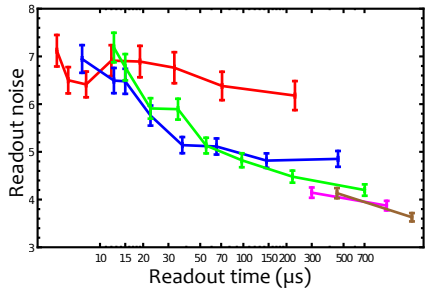

Figure B.5: Measured values of σ_R^{SCC} for a set of powers and times chosen to optimize the readout noise for a photon threshold of 1 photon (red points), 2 photons (blue points), 3 photons (green points), 4 photons (magenta points), or 6 photons (brown points).

2, 3, 4 or 6 photons. The full set of (time, power, threshold) combinations is shown in Fig. B.5. For each value of photon threshold, we used the (time, power) combinations in the range where that photon threshold is optimal, for the data used to fit $\sigma_R^{SCC}(t_R)$.

To find a fit function, we note that for our experimental conditions, $\langle D^- \rangle \gg \langle D^0 \rangle$ and that for short enough readout times, $D^-(n)$ is approximately Poissonian, so that $\sigma_{D^-} \approx \langle D^- \rangle \approx \gamma_1 t_R$:

$$\sigma_R^{SCC} \approx \sqrt{\frac{(\beta_0+\beta_1)(2-\beta_0-\beta_1)}{(\beta_0-\beta_1)^2}} \sqrt{1+\frac{2}{(2-\beta_0-\beta_1)\gamma_1 t_R}}. \tag{B.19}$$

Based on the measured rates and the photon statistics model, the ideal γ_1 was found to scale approximately as $t^{-3/4}$. Therefore, we fitted our measured σ_R^{SCC} values by a function of the form $\sigma_R^{SCC} = a\sqrt{1+b/t^{1/4}}$. The fit parameters were $a = 1.328$ and $b = 39.3$. Although the fitted a is significantly below the $\sigma_{R,best}^{SCC}$ value that we measured under optimal single-shot measurement conditions, the fit nevertheless closely approximates the data and can therefore be used to project the expected magnetometer sensitivity using this method.

References

[1] Y. Chu, N.P. de Leon, B.J. Shields, B. Hausmann, R. Evans, E. Togan, M. J. Burek, M. Markham, A. Stacey, A.S. Zibrov, A. Yacoby, D.J. Twitchen, M. Loncar, H. Park, P. Maletinsky, and M.D. Lukin. Coherent optical transitions in implanted nitrogen vacancy centers. Nano Letters, 14(4):1982–1986, 2014.

[2] Lucio Robledo, Hannes Bernien, Toeno van der Sar, and Ronald Hanson. Spin dynamics in the optical cycle of single nitrogen-vacancy centres in diamond. New Journal of Physics, 13(2):025013, 2011.

[3] E. M. Purcell. Proceedings of the American Physical Society. Physical Review, 69:674–674, June 1946.

[4] Clement Sayrin, Igor Dotsenko, Xingxing Zhou, Bruno Peaudecerf, Theo Rybarczyk, Sebastien Gleyzes, Pierre Rouchon, Mazyar Mirrahimi, Hadis Amini, Michel Brune, Jean-Michel Raimond, and Serge Haroche. Real-time quantum feedback prepares and stabilizes photon number states. Nature, 477(7362):73–77, 09 2011.

[5] J. McKeever, A. Boca, A. D. Boozer, R. Miller, J. R. Buck, A. Kuzmich, and H. J. Kimble. Deterministic generation of single photons from one atom trapped in a cavity. Science, 303(5666):1992–1994, 2004.

[6] Wenlan Chen, Kristin M. Beck, Robert Bücker, Michael Gullans, Mikhail D. Lukin, Haruka Tanji-Suzuki, and Vladan Vuletić. All-optical switch and transistor gated by one stored photon. Science, 341(6147):768–770, 2013.

[7] T. Yoshie, A. Scherer, J. Hendrickson, G. Khitrova, H. M. Gibbs, G. Rupper, C. Ell, O. B. Shchekin, and D. G. Deppe. Vacuum rabi splitting with a single quantum dot in a photonic crystal nanocavity. Nature, 432(7014):200–203, 11 2004.

[8] K. Hennessy, A. Badolato, M. Winger, D. Gerace, M. Atature, S. Gulde, S. Falt, E. L. Hu, and A. Imamoglu. Quantum nature of a strongly coupled single quantum dot-cavity system. Nature, 445(7130):896–899, 02 2007.

[9] Dirk Englund, Andrei Faraon, Ilya Fushman, Nick Stoltz, Pierre Petroff, and Jelena Vuckovic. Controlling cavity reflectivity with a single quantum dot. Nature, 450(7171):857–861, 12 2007.

[10] Andrei Faraon, Charles Santori, Zhihong Huang, Victor M. Acosta, and Raymond G. Beausoleil. Coupling of nitrogen-vacancy centers to photonic crystal cavities in monocrystalline diamond. Phys. Rev. Lett., 109:033604, Jul 2012.

[11] D. Englund, B. Shields, K. Rivoire, F. Hatami, J. Vučković, H. Park, and M. D. Lukin. Deterministic Coupling of a Single Nitrogen Vacancy Center to a Photonic Crystal Cavity. Nano Letters, 10:3922–3926, October 2010.

[12] T. van der Sar, J. Hagemeier, W. Pfaff, E. C. Heeres, S. M. Thon, H. Kim, P. M. Petroff, T. H. Oosterkamp, D. Bouwmeester, and R. Hanson. Deterministic nanoassembly of a coupled quantum emitter-photonic crystal cavity system. Applied Physics Letters, 98(19):193103, May 2011.

[13] Michael Barth, Nils Nüsse, Bernd Löchel, and Oliver Benson. Controlled coupling of a single-diamond nanocrystal to a photonic crystal cavity. Opt. Lett., 34(7):1108–1110, Apr 2009.

[14] Paul E. Barclay, Kai-Mei C. Fu, Charles Santori, Andrei Faraon, and Raymond G. Beausoleil. Hybrid nanocavity resonant enhancement of color center emission in diamond. Phys. Rev. X, 1:011007, Sep 2011.

[15] B. J. M. Hausmann, B. J. Shields, Q. Quan, Y. Chu, N. P. de Leon, R. Evans, M. J. Burek, A. S. Zibrov, M. Markham, D. J. Twitchen, H. Park, M. D. Lukin, and M. Loncăr. Coupling of nv centers to photonic crystal nanobeams in diamond. Nano Letters, 13(12):5791–5796, 2013.

[16] Andrei Faraon, Paul E. Barclay, Charles Santori, Kai-Mei C. Fu, and Raymond G. Beausoleil. Resonant enhancement of the zero-phonon emission from a colour centre in a diamond cavity. Nat Photon, 5(5):301–305, 05 2011.

[17] J. Meijer, S. Pezzagna, T. Vogel, B. Burchard, H.H. Bukow, I.W. Rangelow, Y. Sarov, H. Wiggers, I. Plümel, F. Jelezko, J. Wrachtrup, F. Schmidt-Kaler, W. Schnitzler, and K. Singer. Towards the implanting of ions and positioning of nanoparticles with nm spatial resolution. Applied Physics A, 91(4):567–571, 2008.

[18] J. M. Taylor, P. Cappellaro, L. Childress, L. Jiang, D. Budker, P. R. Hemmer, A. Yacoby, R. Walsworth, and M. D. Lukin. High-sensitivity diamond magnetometer with nanoscale resolution. Nat Phys, 4(10):810–816, 10 2008.

[19] J. R. Maze, P. L. Stanwix, J. S. Hodges, S. Hong, J. M. Taylor, P. Cappellaro, L. Jiang, M. V. Gurudev Dutt, E. Togan, A. S. Zibrov, A. Yacoby, R. L. Walsworth, and M. D. Lukin. Nanoscale magnetic sensing with an individual electronic spin in diamond. Nature, 455(7213):644–647, 10 2008.

[20] Gopalakrishnan Balasubramanian, I. Y. Chan, Roman Kolesov, Mohannad Al-Hmoud, Julia Tisler, Chang Shin, Changdong Kim, Aleksander Wojcik, Philip R. Hemmer, Anke Krueger, Tobias Hanke, Alfred Leitenstorfer, Rudolf Bratschitsch, Fedor Jelezko, and Jorg Wrachtrup. Nanoscale imaging magnetometry with diamond spins under ambient conditions. Nature, 455(7213):648–651, 10 2008.

[21] F. Dolde, H. Fedder, M. W. Doherty, T. Nobauer, F. Rempp, G. Balasubramanian, T. Wolf, F. Reinhard, L. C. L. Hollenberg, F. Jelezko, and J. Wrachtrup. Electric-field sensing using single diamond spins. Nat Phys, 7(6):459–463, 06 2011.

[22] Gopalakrishnan Balasubramanian, Philipp Neumann, Daniel Twitchen, Matthew Markham, Roman Kolesov, Norikazu Mizuochi, Junichi Isoya, Jocelyn Achard, Johannes Beck, Julia Tissler, Vincent Jacques, Philip R. Hemmer, Fedor Jelezko, and Jorg Wrachtrup. Ultralong spin coherence time in isotopically engineered diamond. Nat Mater, 8(5):383–387, 05 2009.

[23] Boris Naydenov, Friedemann Reinhard, Anke Lämmle, V. Richter, Rafi Kalish, Ulrika F. S. D?Haenens-Johansson, Mark Newton, Fedor Jelezko, and Jörg Wrachtrup. Increasing the coherence time of single electron spins in diamond by high temperature annealing. 97(24):242511, 2010.

[24] G. de Lange, Z. H. Wang, D. Ristè, V. V. Dobrovitski, and R. Hanson. Universal dynamical decoupling of a single solid-state spin from a spin bath. Science, 330(6000):60–63, 2010.

[25] Boris Naydenov, Florian Dolde, Liam T. Hall, Chang Shin, Helmut Fedder, Lloyd C. L. Hollenberg, Fedor Jelezko, and Jörg Wrachtrup. Dynamical decoupling of a single-electron spin at room temperature. Phys. Rev. B, 83:081201, Feb 2011.

[26] C. A. Ryan, J. S. Hodges, and D. G. Cory. Robust decoupling techniques to extend quantum coherence in diamond. Phys. Rev. Lett., 105:200402, Nov 2010.

[27] C. J. Hood, T. W. Lynn, A. C. Doherty, A. S. Parkins, and H. J. Kimble. The atom-cavity microscope: Single atoms bound in orbit by single photons. Science, 287(5457):1447–1453, 2000.

[28] Andrea M. Armani, Rajan P. Kulkarni, Scott E. Fraser, Richard C. Flagan, and Kerry J. Vahala. Label-free, single-molecule detection with optical microcavities. Science, 317(5839):783–787, 2007.

[29] Kartik Srinivasan and Oskar Painter. Linear and nonlinear optical spectroscopy of a strongly coupled microdisk-quantum dot system. Nature, 450(7171):862–865, 12 2007.

[30] Masayuki Fujita, Shigeki Takahashi, Yoshinori Tanaka, Takashi Asano, and Susumu Noda. Simultaneous inhibition and redistribution of spontaneous light emission in photonic crystals. Science, 308(5726):1296–1298, 2005.

[31] D. Englund, D. Fattal, E. Waks, G. Solomon, B. Zhang, T. Nakaoka, Y. Arakawa, Y. Yamamoto, and J. Vučković. Controlling the Spontaneous Emission Rate of Single Quantum Dots in a Two-Dimensional Photonic Crystal. Physical Review Letters, 95(1):013904, July 2005.

[32] Stefan Strauf, Nick G. Stoltz, Matthew T. Rakher, Larry A. Coldren, Pierre M. Petroff, and Dirk Bouwmeester. High-frequency single-photon source with polarization control. Nat Photon, 1(12):704–708, 12 2007.

[33] J. I. Cirac, P. Zoller, H. J. Kimble, and H. Mabuchi. Quantum state transfer and entanglement distribution among distant nodes in a quantum network. Phys. Rev. Lett., 78:3221–3224, Apr 1997.

[34] H.-J. Briegel, W. Dür, J. I. Cirac, and P. Zoller. Quantum repeaters: The role of imperfect local operations in quantum communication. Phys. Rev. Lett., 81:5932–5935, Dec 1998.

[35] Paul E. Barclay, Kai-Mei Fu, Charles Santori, and Raymond G. Beausoleil. Hybrid photonic crystal cavity and waveguide for coupling to diamond nv-centers. Opt. Express, 17(12):9588–9601, Jun 2009.

[36] Igal Bayn and Joseph Salzman. Ultra high-q photonic crystal nanocavity design: The effect of a low-ϵ slab material. Opt. Express, 16(7):4972–4980, Mar 2008.

[37] Christine Kreuzer, Janine Riedrich-Möller, Elke Neu, and Christoph Becher. Design of photonic crystal microcavities in diamond films. Opt. Express, 16(3):1632–1644, Feb 2008.

[38] P. Neumann, N. Mizuochi, F. Rempp, P. Hemmer, H. Watanabe, S. Yamasaki, V. Jacques, T. Gaebel, F. Jelezko, and J. Wrachtrup. Multipartite entanglement among single spins in diamond. Science, 320(5881):1326–1329, 2008.

[39] L. Jiang, J. S. Hodges, J. R. Maze, P. Maurer, J. M. Taylor, D. G. Cory, P. R. Hemmer, R. L. Walsworth, A. Yacoby, A. S. Zibrov, and M. D. Lukin. Repetitive readout of a single electronic spin via quantum logic with nuclear spin ancillae. Science, 326(5950):267–272, 2009.

[40] G. D. Fuchs, V. V. Dobrovitski, D. M. Toyli, F. J. Heremans, and D. D. Awschalom. Gigahertz dynamics of a strongly driven single quantum spin. Science, 326(5959):1520–1522, 2009.

[41] Yoshihiro Akahane, Takashi Asano, Bong-Shik Song, and Susumu Noda. High-q photonic nanocavity in a two-dimensional photonic crystal. Nature, 425(6961):944–947, 10 2003.

[42] Kelley Rivoire, Andrei Faraon, and Jelena Vuckovic. Gallium phosphide photonic crystal nanocavities in the visible. Applied Physics Letters, 93(6):–, 2008.

[43] A.P. Nizovtsev, S.Ya. Kilin, C. Tietz, F. Jelezko, and J. Wrachtrup. Modeling fluorescence of single nitrogen–vacancy defect centers in diamond. Physica B: Condensed Matter, 308–310(0):608 – 611, 2001. International Conference on Defects in Semiconductors.

[44] Paul E. Barclay, Charles Santori, Kai-Mei Fu, Raymond G. Beausoleil, and Oskar Painter. Coherent interference effects in a nano-assembled diamond nv center cavity-qed system. Opt. Express, 17(10):8081–8097, May 2009.

[45] Jacob T. Robinson, Christina Manolatou, Long Chen, and Michal Lipson. Ultrasmall mode volumes in dielectric optical microcavities. Phys. Rev. Lett., 95:143901, Sep 2005.

[46] W. E. Moerner. A dozen years of single-molecule spectroscopy in physics, chemistry, and biophysics. The Journal of Physical Chemistry B, 106(5):910–927, 2002.

[47] H. K. Pulker. Characterization of optical thin films. Appl. Opt., 18(12):1969–1977, Jun 1979.

[48] Séverine Diziain, Jean-Marc Merolla, Michel Spajer, Giacomo Benvenuti, Ali Dabirian, Yury Kuzminykh, Patrik Hoffmann, and Maria-Pilar Bernal. Determination of local refractive index variations in thin films by heterodyne interferometric scanning near-field optical microscopy. Review of Scientific Instruments, 80(9):–, 2009.

[49] H. J. Kimble. The quantum internet. Nature, 453(7198):1023–1030, 06 2008/06/19/print.

[50] A.M. Zaitsev. Optical Properties of Diamond: A Data Handbook. Springer, 2001.

[51] L.I. Childress. Coherent Manipulation of Single Quantum Systems in the Solid State. Harvard University, 2007.

[52] Jörg Wrachtrup and Fedor Jelezko. Processing quantum information in diamond. Journal of Physics: Condensed Matter, 18(21):S807, 2006.

[53] Jeremy L. O'Brien. Optical quantum computing. Science, 318(5856):1567–1570, 2007.

[54] MaletinskyP., HongS., GrinoldsM. S., HausmannB., LukinM. D., WalsworthR. L., LoncarM., and YacobyA. A robust scanning diamond sensor for nanoscale imaging with single nitrogen-vacancy centres. Nat Nano, 7(5):320–324, 05 2012.

[55] L. Childress, J. M. Taylor, A. S. Sørensen, and M. D. Lukin. Fault-tolerant quantum communication based on solid-state photon emitters. Phys. Rev. Lett., 96:070504, Feb 2006.

[56] Alexios Beveratos, Rosa Brouri, Thierry Gacoin, André Villing, Jean-Philippe Poizat, and Philippe Grangier. Single photon quantum cryptography. Phys. Rev. Lett., 89:187901, Oct 2002.

[57] J. P. Reithmaier, G. Sek, A. Loffler, C. Hofmann, S. Kuhn, S. Reitzenstein, L. V. Keldysh, V. D. Kulakovskii, T. L. Reinecke, and A. Forchel. Strong coupling in a single quantum dot-semiconductor microcavity system. Nature, 432(7014):197–200, 11 2004.

[58] Dirk Englund, Brendan Shields, Kelley Rivoire, Fariba Hatami, Jelena Vučković, Hongkun Park, and Mikhail D. Lukin. Deterministic coupling of a single nitrogen vacancy center to a photonic crystal cavity. Nano Letters, 10(10):3922–3926, 2010.

[59] Janik Wolters, Andreas W. Schell, Günter Kewes, Nils Nüsse, Max Schoengen, Henning Döscher, Thomas Hannappel, Bernd Löchel, Michael Barth, and Oliver Benson. Enhancement of the zero phonon line emission from a single nitrogen vacancy center in a nanodiamond via coupling to a photonic crystal cavity. Applied Physics Letters, 97(14):–, 2010.

[60] T. van der Sar, J. Hagemeier, W. Pfaff, E. C. Heeres, S. M. Thon, H. Kim, P. M. Petroff, T. H. Oosterkamp, D. Bouwmeester, and R. Hanson. Deterministic nanoassembly of a coupled quantum emitter–photonic crystal cavity system. Applied Physics Letters, 98(19):–, 2011.

[61] Nathalie P. de Leon, Brendan J. Shields, Chun L. Yu, Dirk E. Englund, Alexey V. Akimov, Mikhail D. Lukin, and Hongkun Park. Tailoring light-matter interaction with a nanoscale plasmon resonator. Phys. Rev. Lett., 108:226803, May 2012.

[62] Birgit J. M. Hausmann, Brendan Shields, Qimin Quan, Patrick Maletinsky, Murray McCutcheon, Jennifer T. Choy, Tom M. Babinec, Alexander Kubanek, Amir Yacoby, Mikhail D. Lukin, and Marko Lončar. Integrated diamond networks for quantum nanophotonics. Nano Letters, 12(3):1578–1582, 2012.

[63] Janine Riedrich-Moller, Laura Kipfstuhl, Christian Hepp, Elke Neu, Christoph Pauly, Frank Mucklich, Armin Baur, Michael Wandt, Sandra Wolff, Martin Fischer, Stefan Gsell, Matthias Schreck, and Christoph Becher. One- and two-dimensional photonic crystal microcavities in single crystal diamond. Nat Nano, 7(1):69–74, 01 2012.

[64] Michael J. Burek, Nathalie P. de Leon, Brendan J. Shields, Birgit J. M. Hausmann, Yiwen Chu, Qimin Quan, Alexander S. Zibrov, Hongkun Park, Mikhail D. Lukin, and Marko Lončar. Free-standing mechanical and photonic nanostructures in single-crystal diamond. Nano Letters, 12(12):6084–6089, 2012.

[65] Byeong-Hyeon Ahn, Ju-Hyung Kang, Myung-Ki Kim, Jung-Hwan Song, Bumki Min, Ki-Soo Kim, and Yong-Hee Lee. One-dimensional parabolic-beam photonic crystal laser. Opt. Express, 18(6):5654–5660, Mar 2010.

[66] Qimin Quan and Marko Loncar. Deterministic design of wavelength scale, ultra-high q photonic crystal nanobeam cavities. Opt. Express, 19(19):18529–18542, Sep 2011.

[67] Qimin Quan, Parag B. Deotare, and Marko Loncar. Photonic crystal nanobeam cavity strongly coupled to the feeding waveguide. Applied Physics Letters, 96(20):–, 2010.

[68] H. J. Kimble, M. Dagenais, and L. Mandel. Photon antibunching in resonance fluorescence. Phys. Rev. Lett., 39:691–695, Sep 1977.

[69] S. Mosor, J. Hendrickson, B. C. Richards, J. Sweet, G. Khitrova, H. M. Gibbs, T. Yoshie, A. Scherer, O. B. Shchekin, and D. G. Deppe. Scanning a photonic crystal slab nanocavity by condensation of xenon. Applied Physics Letters, 87(14):–, 2005.

[70] Kyu Young Han, Seong Keun Kim, Christian Eggeling, and Stefan W. Hell. Metastable dark states enable ground state depletion microscopy of nitrogen vacancy centers in diamond with diffraction-unlimited resolution. Nano Letters, 10(8):3199–3203, 2010.

[71] K Y Han, D Wildanger, E Rittweger, J Meijer, S Pezzagna, S W Hell, and C Eggeling. Dark state photophysics of nitrogen–vacancy centres in diamond. New Journal of Physics, 14(12):123002, 2012.

[72] G. Waldherr, J. Beck, M. Steiner, P. Neumann, A. Gali, Th. Frauenheim, F. Jelezko, and J. Wrachtrup. Dark states of single nitrogen-vacancy centers in diamond unraveled by single shot nmr. Phys. Rev. Lett., 106:157601, Apr 2011.

[73] K. Beha, A. Batalov, N. B. Manson, R. Bratschitsch, and A. Leitenstorfer. Optimum photoluminescence excitation and recharging cycle of single nitrogen-vacancy centers in ultrapure diamond. Phys. Rev. Lett., 109:097404, Aug 2012.

[74] N Aslam, G Waldherr, P Neumann, F Jelezko, and J Wrachtrup. Photo-induced ionization dynamics of the nitrogen vacancy defect in diamond investigated by single-shot charge state detection. New Journal of Physics, 15(1):013064, 2013.

[75] A. Gruber, A. Dräbenstedt, C. Tietz, L. Fleury, J. Wrachtrup, and C. von Borczyskowski. Scanning confocal optical microscopy and magnetic resonance on single defect centers. Science, 276(5321):2012–2014, 1997.

[76] E. L. Hahn. Spin echoes. Phys. Rev., 80:580–594, Nov 1950.

[77] J R Maze, A Gali, E Togan, Y Chu, A Trifonov, E Kaxiras, and M D Lukin. Properties of nitrogen-vacancy centers in diamond: the group theoretic approach. New Journal of Physics, 13(2):025025, 2011.

[78] Stefan Schietinger, Tim Schröder, and Oliver Benson. One-by-one coupling of single defect centers in nanodiamonds to high-q modes of an optical microresonator. Nano Letters, 8(11):3911–3915, 2008.

[79] N. B. Manson, J. P. Harrison, and M. J. Sellars. Nitrogen-vacancy center in diamond: Model of the electronic structure and associated dynamics. Phys. Rev. B, 74:104303, Sep 2006.

[80] L. Childress, M. V. Gurudev Dutt, J. M. Taylor, A. S. Zibrov, F. Jelezko, J. Wrachtrup, P. R. Hemmer, and M. D. Lukin. Coherent dynamics of coupled electron and nuclear spin qubits in diamond. Science, 314(5797):281–285, 2006.

[81] Alexia Auffèves, Jean-Michel Gérard, and Jean-Philippe Poizat. Pure emitter dephasing: A resource for advanced solid-state single-photon sources. Phys. Rev. A, 79:053838, May 2009.

This thesis was typeset using LaTeX, originally developed by Leslie Lamport and based on Donald Knuth's TeX. ~~The body text is set in 11 point Egenolff-Berner Garamond, a revival of Claude Garamont's humanist typeface.~~ A template that can be used to format a PhD thesis with this look and feel has been released under the permissive MIT (X11) license, and can be found online at github.com/suchow/Dissertate or from its author, Jordan Suchow, at suchow@post.harvard.edu.

The original template has been modified to reflect a more "normal" thesis look.